LITHOS 522-523 (2026) 108389

Contents lists available at ScienceDirect

LITHOS

journal homepage: www.elsevier.com/locate/lithos

Mesozoic magmatism in the Andes of southern Ecuador and northern Peru: Tectonic insights from whole-rock chemistry and zircon petrochronology

Leidy Carolina Sandoval Espinel [a,b,*], Cesar Witt [b], Jorge Iglesias [b], Massimiliano Zattin [a], Olivier Bruguier [c], Marc Poujol [d], Pablo Samaniego [e], Mauricio Bermudez [f], John Jairo Sandoval Espinel [f,g]

[a] University of Padova, Geosciences Department, Via Giotto 1, 35137 Padua, Italy
[b] Univ. Lille, CNRS, IRD, Univ. Littoral Côte d'Opale, UMR 8187, LOG, Laboratoire d'Océanologie et de Géosciences, F 59000 Lille, France
[c] University of Montpellier, CNRS, Géosciences Montpellier, 34095 Montpellier, France
[d] University of Rennes, CNRS, Géosciences Rennes, UMR6118, F-35000 Rennes, France
[e] University of Clermont Auvergne, CNRS-IRD, Laboratoire Magmas et Volcans, 63170 Clermont-Ferrand, France
[f] Pedagogical and technological university of Colombia, School of Geological Engineering, 152211 Sogamoso, Colombia
[g] Potosino Institute for Scientific and Technological Research (IPICYT), Applied Geosciences Division, Camino a la Presa San José, 78216 San Luis Potosí, Mexico

ARTICLE INFO

Keywords:
Northern Andes
Zircon petrochronology
Hf–O isotopes
Subduction magmatism

ABSTRACT

The southern Ecuador–northern Peru region marks the transition between the northern and central Andes. This study reconstructs the Mesozoic magmatic history of this key region by integrating petrography, U—Pb geochronology, whole-rock and zircon geochemistry, and $\varepsilon Hf_{(t)}$ and $\delta^{18}O$ zircon isotopic data from plutonic rocks. Our results indicate that much of the Mesozoic magmatism occurred in an extensional arc setting, with magmatic reservoirs progressively incorporating more depleted, mantle material, while crustal contributions diminished through time. Magmatic reservoirs evolved both spatially and temporally, beginning with an extensive Triassic arc dominated by granitoids exhibiting strong crustal signatures at least until 220 Ma. This was followed by mildly enriched signatures associated with a stationary Jurassic to Early Cretaceous arc active between ~190 and ~ 126 Ma. Somewhere in between 126 and 104 Ma, the arc underwent a significant westward migration, potentially driven by slab rollback, which coincided with the opening of the Celica–Lancones Basin and the subsequent emplacement of the Late Cretaceous Celica–Lancones arc onto oceanic basement. This migration is consistent with westward shifts observed in central Ecuador and Colombia but contrasts with coeval eastward migration documented in central and southern Peru. In addition, new U—Pb ages challenge current interpretations of a missing Jurassic arc in northern Peru by providing clear evidence that Jurassic magmatism extended at least as far south as 6°S.

1. Introduction

The evolution of arc magmatism at convergent margins is governed by complex interactions between subduction dynamics, mantle flow, and tectonic processes. Variations in slab geometry, including changes in dip, rollback, and flat-slab development, strongly influence mantle wedge circulation, melt generation, and the thermal structure of the overriding lithosphere (Ducea et al., 2015). These processes exert control over the spatial and temporal distribution of magmatic arcs. For instance, observed trenchward or landward arc migration, as well as intervals of magmatic quiescence, are commonly interpreted as the surface expression of such changes in subduction geometry. Documenting these shifts through time is therefore fundamental for reconstructing the tectonomagmatic evolution of long-lived subduction systems.

The Andean belt developed above the subduction margin of the oceanic Nazca Plate (formerly part of the Farallon Plate) beneath the South American continent (DeCelles et al., 2009). Its northern segment records a particularly intricate evolution, shaped by the accretion of oceanic terranes, changes in subduction direction, episodic magmatism, and multiple exhumation events (Iglesias et al., 2025; Jaillard, 2025; Spikings et al., 2010; Spikings et al., 2015; Vallejo et al., 2009; Witt

---

* Corresponding author at: University of Padova, Geosciences Department, Via Giotto 1, 35137 Padua, Italy.
E-mail address: leidycarolina.sandovalespinel@studenti.unipd.it (L.C. Sandoval Espinel).

https://doi.org/10.1016/j.lithos.2025.108389
Received 19 August 2025; Received in revised form 20 December 2025; Accepted 20 December 2025
Available online 26 December 2025
0024-4937/© 2025 The Authors. Published by Elsevier B.V. This is an open access article under the CC BY license (http://creativecommons.org/licenses/by/4.0/).

et al., 2023). Despite recent advances in reconstructing the long-term magmatic and tectonic evolution of the Northern Andes (Boekhout et al., 2012; Carrasco et al., 2023; Chavarría et al., 2022; Cochrane et al., 2014; Duan et al., 2022; Jaillard, 2022; Pratt et al., 2005; Riel et al., 2014; Sandoval-Espinel et al., 2025; Vallejo et al., 2009; Winter et al., 2010; Witt et al., 2017), the southernmost part, encompassing southern Ecuador and northern Peru, remains poorly understood and is still subject to contrasting interpretations (see Bustamante et al., 2016; Cochrane et al., 2014; Spikings et al., 2015).

These uncertainties primarily reflect the limited availability of high-precision geochronological datasets. Most of the existing age constraints in this region are derived from the ^{40}Ar—^{39}Ar and K—Ar analyses of minerals such as muscovite, hornblende, and biotite (e.g., Baldock, 1977; Cochrane et al., 2014; Feininger & Silberman, 1982; Hama, 1990; Litherland, 1994; Spikings et al., 2010; Winter, 2008; Table S1; Fig. S1). While these datasets have provided valuable temporal references, they are often affected by thermal resetting and may not accurately reflect magmatic crystallization ages. In contrast, zircon U—Pb dating offers a more robust chronometer, as zircon is a refractory and chemically resistant mineral that usually retains the composition of its parent magma during subsequent metamorphic or hydrothermal processes. Furthermore, when zircon U—Pb ages are combined with zircon

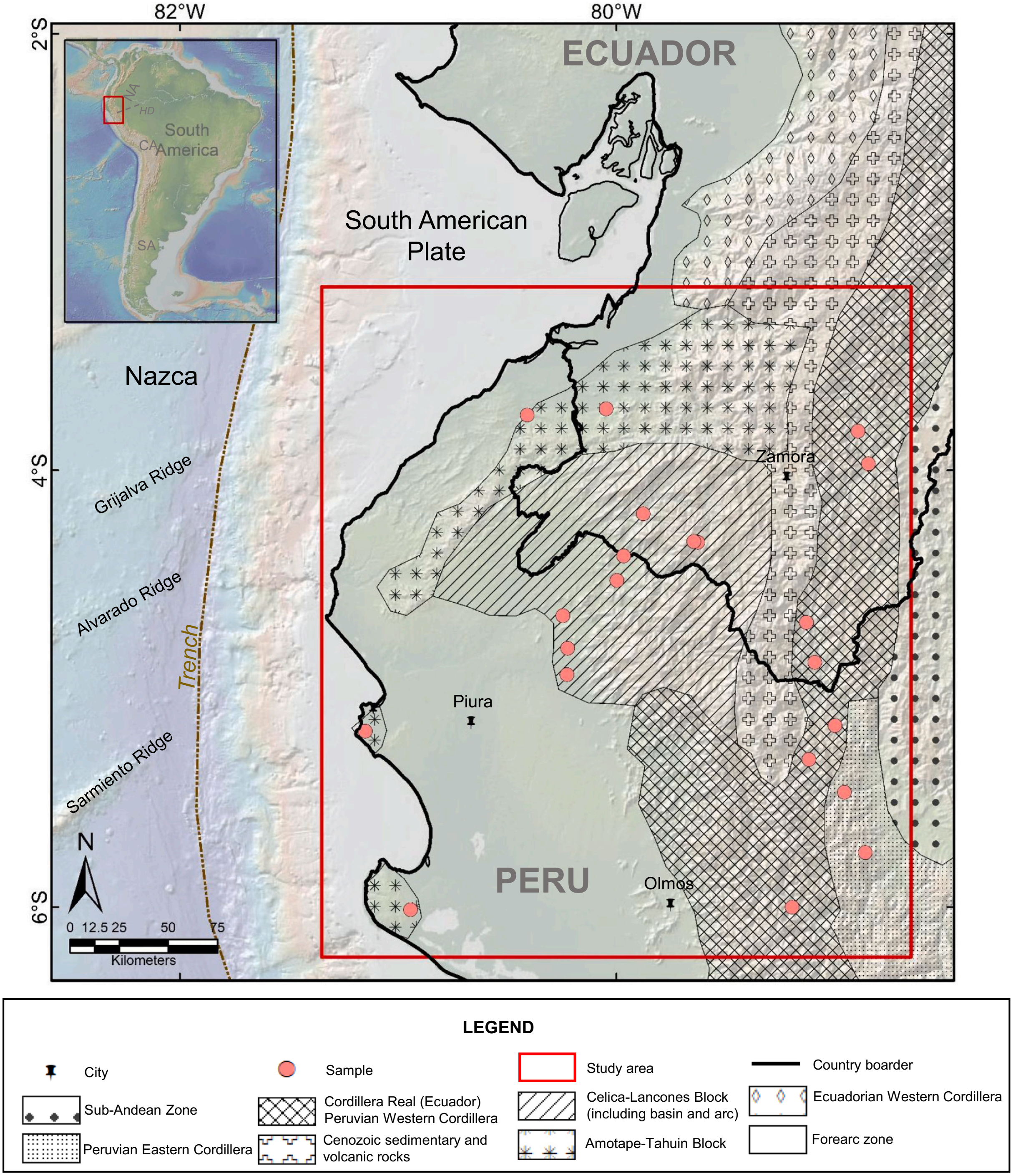

Fig. 1. Geological sketch of northern Peru and Ecuador, showing major units, the study area, and sample locations. CA: Central Andes. HD: Huancabamba Deflection. NA: Northern Andes. SA: Southern Andes.

geochemistry and Hf—O isotopic data, both the timing of magmatism and the nature of magma sources can be constrained simultaneously. However, such high-precision and integrated datasets remain extremely scarce in southern Ecuador and northern Peru, limiting our ability to test competing Mesozoic evolutionary models for this region (e.g., Duan et al., 2022; Spikings et al., 2015), and to accurately constrain the spatiotemporal evolution of magmatism and its sources in this segment of the Andes.

This study integrates U—Pb zircon geochronology, petrographic analysis, and whole-rock and zircon geochemistry for plutonic rocks from the southernmost Northern Andes (~4–6°S). Our new data refine the temporal and geochemical evolution of Mesozoic magmatism in southern Ecuador and northern Peru between 240 and 90 Ma. These results allow us to reassess the timing of arc migration and to propose an updated tectonomagmatic model linked to changes in magmatic reservoirs.

2. Geotectonic framework

2.1. Tectonic background

The Northern Andes spans from Venezuela to northern Peru (Jaillard et al., 1990). The region is separated from the Central Andes by the Huancabamba Deflection, located at approximately 6°S. This zone marks a change in the orientation of the Andean chain from N20°E in the north to N20°W in the south (Fig. 1). Magmatic activity along the Northern Andes is driven by the interaction between the South American Plate with a series of oceanic plate systems, producing a long-lived subduction system characterized by episodic magmatism from the Carboniferous to the Holocene (Horton, 2018; Jaillard et al., 2000).

During the early Mesozoic, the western South American margin was subjected to an extensional regime contemporaneous with voluminous magmatic activity between ~265 and ~ 215 Ma (Leal-Mejía et al., 2019; and references therein). This magmatism was driven by prolonged high mantle heat flow and crustal anatexis (e.g., Cochrane et al., 2014; Riel et al., 2018). Models proposed for this Triassic magmatic event during the breakup of Pangea can be broadly classified into: (i) those that interpret magmatism as arising from non-subduction processes (Fig. 2; Carrillo et al., 2021; Cochrane et al., 2014; Spikings et al., 2015) and (ii) those invoking active subduction (e.g., Riel et al., 2018; Villares et al., 2020). Regardless of the model, studies have shown that crustal reworking during this period resulted in the formation of S-type Triassic granitoids emplaced along the Real Cordillera (including the Sub-Andean zone) and the Amotape–Tahuin block (ATB) in Ecuador (Fig. 1; Aspen et al., 1992; Litherland, 1994; Riel et al., 2014; Sandoval-Espinel et al., 2025; Spikings et al., 2015) as well as in the southern and central segments of the Peruvian Eastern Cordillera (Mišković et al., 2009).

Subsequently, two competing hypotheses have been proposed for the Jurassic evolution of the margin. In the first scenario, subduction was re-established between ~209 and ~ 190 Ma (Cochrane et al., 2014), marking the onset of a new continental arc along the South American margin. Alternatively, in the second scenario, oceanic subduction may have continued uninterrupted since the Triassic (Villares et al., 2020).

From both hypotheses, it is agreed that during the Jurassic, the Northern Andes experienced an extensional regime. This setting has been attributed to either (i) highly oblique convergence (Bustamante et al., 2016; Jaillard et al., 1990), or (ii) slab rollback, which drove the westward migration of the arc between 189 and 141 Ma from the present-day Cordillera Real to the Western Cordillera (Fig. 1; Cochrane et al., 2014; Spikings et al., 2015). The Jurassic arc extends across much of the Northern Andes, with older crystallization ages (209–196 Ma) recorded in northern Colombia (e.g., Santander and Santa Marta massifs; Van der Lelij, 2013; Villagómez et al., 2011), while younger ages

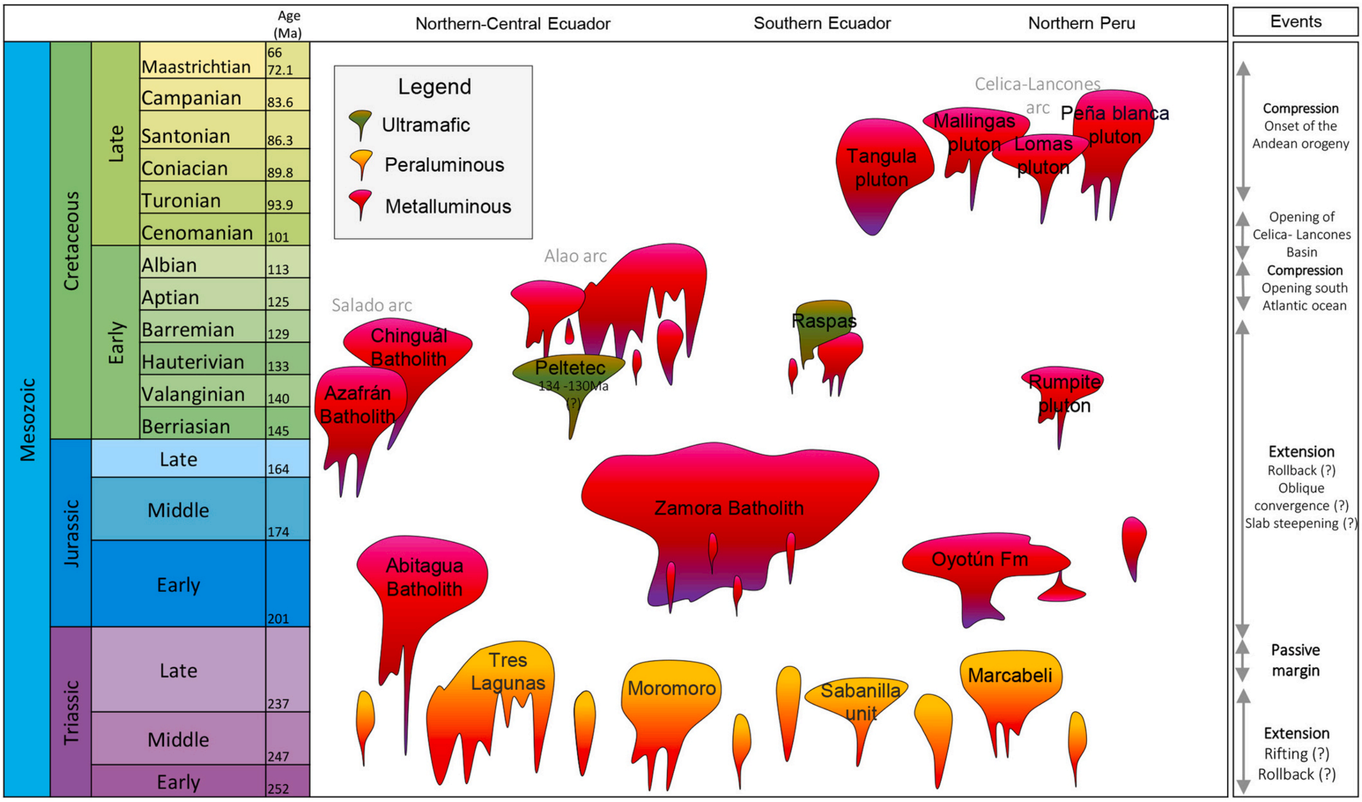

Fig. 2. (A) Overview of the Spatiotemporal distribution of Mesozoic magmatism in Ecuador and northern Peru, along with key tectonic and geodynamic events. The figure is based on data from CGS-INGEMMET (2017), Cochrane et al. (2014), Feininger and Silberman (1982), Hama (1990), Litherland et al. (1994), Noble et al. (1997), Schutte et al. (2010), Spikings et al. (2010), Ulrich (2005), Winter (2008), Sandoval- Espinel et al. (2025), and this study.

(180–132 Ma) are reported in Ecuador (e.g., Ambitagua and Zamora batholiths; Chiaradia, 2009; Cochrane et al., 2014). This distribution has been interpreted as a general southward-younging magmatic trend from northern Colombia to southern Ecuador (e.g., Spikings et al., 2015). In addition, Jurassic magmatism appears to be absent between 5°S and 12°S, either because an arc never formed in this region or because it was removed by subduction or erosion (Boekhout et al., 2012; Spikings et al., 2015).

The extensional regime persisted until the Early Cretaceous, contemporaneous with emplacement of the Peruvian Coastal Batholith within the Western Cordillera of Peru (Boekhout et al., 2012; Cochrane et al., 2014; Mišković et al., 2009) as well as the formation of the Salado and Alao arcs in Ecuador (Fig. 3; Carrasco et al., 2023). The Salado Arc is located in northern and central Ecuador and consists of scattered metaluminous granitoids, such as the Azafrán Batholith (~145–140 Ma; Cochrane et al., 2014) and the Chingual Pluton (~125 Ma; Spikings et al., 2015). The Alao Arc, located west of the Salado Arc, is composed of two distinct rock assemblages: (i) metaluminous volcanic rocks, formed between ~140 and 110 Ma (Carrasco et al., 2023), and (ii) the *E*-MORB-like basalts of the Peltetec Complex (130–134 Ma; Gabriele, 2002; Spikings et al., 2015). Notably, rocks with lithological similarities to these E-MORB-like basalts have been identified in the ophiolitic succession of the Raspas Complex in southern Ecuador (130–120 Ma), which has undergone metamorphism under blueschist to eclogite facies conditions (Gabriele, 2002; Riel et al., 2014). It should be noted, however, that recent U—Pb dating suggests that some units previously identified as Early Cretaceous in central Ecuador (west of the older arcs), such as the Peltetec Complex, may instead be Triassic in age (~228 Ma; Villares et al., 2020).

It is likely that the continuation of the extensional setting promoted the opening of the NE–SW Celica–Lancones Basin, situated between the Early Cretaceous volcanic arc and the ATB, as evidenced by rift-related volcanism within the basin (Jaillard et al., 1999; Mourier, 1988; Winter et al., 2010). Basalt-dominated volcanism dated at 104.8 ± 1.3 to 100.2 ± 0.5 Ma (Winter et al., 2010) marked the deep rifting stage of the basin and suggests that its onset is at least middle Albian in age.

Around ~100 Ma, active seafloor spreading in the South Atlantic and the resulting westward drift of the South American Plate triggered a tectonic shift from extension to compression (Jaillard, 2025; and references therein). This transition led to the development of the Early to Late Cretaceous Celica–Lancones Arc (~110–78 Ma; Schütte et al., 2010; Soler, 1991; Winter, 2008), which extends across southern Ecuador and northern Peru (Figs. 1 and 3). This arc is mainly composed of andesitic lavas, pyroclastic deposits, and intrusive bodies, including the Tangula pluton in southern Ecuador and the Peña Blanca, Lomas, and Mallingas plutons in northern Peru (Fig. 2; Schütte et al., 2010; Winter, 2008). Due to the limited geochemical and geochronological constraints in this region, the Celica–Lancones Arc has been tentatively genetically linked to the subduction system that formed the Alao Arc (Jaillard et al., 1999; Spikings et al., 2015). Further south, in central and southern Peru, evidence of this compressional regime is recorded by localized folding and faulting, the cessation of marine sedimentation, and the widespread emplacement of large intrusive bodies that contributed to the final stages of the formation of the Peruvian Coastal Batholith (Martínez-Ardila et al., 2023; and references therein).

3. Analytical methods

Nineteen samples were obtained from igneous outcrops located between 3.5 and 6°S in southern Ecuador and northern Peru. Sample locations and their corresponding nomenclature are provided in Table S2 and illustrated in Fig. 3.

3.1. Petrographic analyses

Twelve samples were selected for petrographic analyses. Hence, rocks were cut using a diamond saw and then ground and polished until they reached a thickness of about 30 μm, employing progressively finer abrasives. Posteriorly, thin sections were examined at 50-500× magnification using a Leica petrographic microscope and photographed under plane and cross-polarized transmitted light at Padova University. Results are shown in Table S3 and Fig. 4.

3.2. LA-ICP-MS zircon U—Pb dating

Zircons were separated by crushing, sieving, magnetic and heavy liquid concentration at the laboratory of thermochronology in the Universidad Pedagógica y Tecnológica de Colombia, UPTC. Subsequently, hand-picked and mounted in epoxy blocks and polished on a lap wheel with a 9 μm, 6 μm and 3 μm diamond suspension successively, until revel crystal surfaces.

Cathodoluminescence (CL) imaging was performed in order to recognize different micro-area compositional heterogenies within a crystal before analysis (Fig. S2). Imaging acquisition was performed using a cold cathodoluminescence model 8200 MkII equipment mounted in an Olympus BX41 microscope at Lille university.

Zircon U—Pb dating was conducted using a LA-ICP-MS at the GeOHeLiS analytical platform (OSUR, Univ. Rennes) using an ESI NWR193UC Excimer laser coupled to a quadrupole Agilent 7700× ICP-MS equipped with a dual pumping system to enhance sensitivity. The instrumental setup is presented in Table S4. Additional information can be found in Witt et al. (2017).

Data was analyzed using the ISOPLOT package program; ^{206}Pb/^{238}U dates were used since zircons are younger than 1Ga. We only report concordant ages (90 % to 110 % concordance), while, errors are reported at 2 sigma level. U—Pb data and calculated ages can be found in table S5, while quality control reference materials data (Plešovice and GJ1) are on Tables S6 and S7, respectively. Representative concordia and weighted diagrams are presented in Fig. 5.

3.3. ICP-AES whole rock geochemistry

Samples were washed with distilled water to remove impurities. Fresh, unaltered portions were then selected and crushed at Lille university using an agate mortar pulverizer to obtain a < 50 mesh size fraction. This portion was further pulverized using an agate ball mill to achieve a particle size of <10 μm.

Whole-rock major and trace elements were determined for fifteen samples at the Institut Universitaire Européen de la Mer, Université de Bretagne Occidentale (Brest, France) using a Jobin Yvon Ultima 2 inductively coupled plasma atomic emission spectrometer (ICP-AES). Sample preparation followed the procedure outlined by Cotten et al. (1995), which included digestion with HF and HNO_3, neutralization with boric acid, and subsequent dilution in nitric acid. Calibration was performed using international standards (AC-E, BEN, JB-2, PM-S, and WS-E) along with internal standards (MORB-E, CB2, CB15, and CB18), ensuring reliable external reproducibility. Relative standard deviations are <2 %, except for low values (< 0.50 wt%), for which the absolute standard deviation is ±0.01 wt%.

The geochemical data were processed using the IgRoCS computer program (Verma and Rivera-Gómez, 2013). This software accurately partitions total iron into its two oxidation states (FeO and Fe_2O_3) and normalizes the sum of major oxides to 100 % on an anhydrous basis. Major and trace element concentrations are listed in Table S8.

3.4. Hafnium analysis

Hafnium isotopic compositions of zircon are largely controlled by the time elapsed since a melt is removed from the mantle, whereby recently removed melts display more juvenile isotopic signatures than rocks with longer crustal residence time.

Lu—Hf isotopes analysis were performed at Géosciences Montpellier

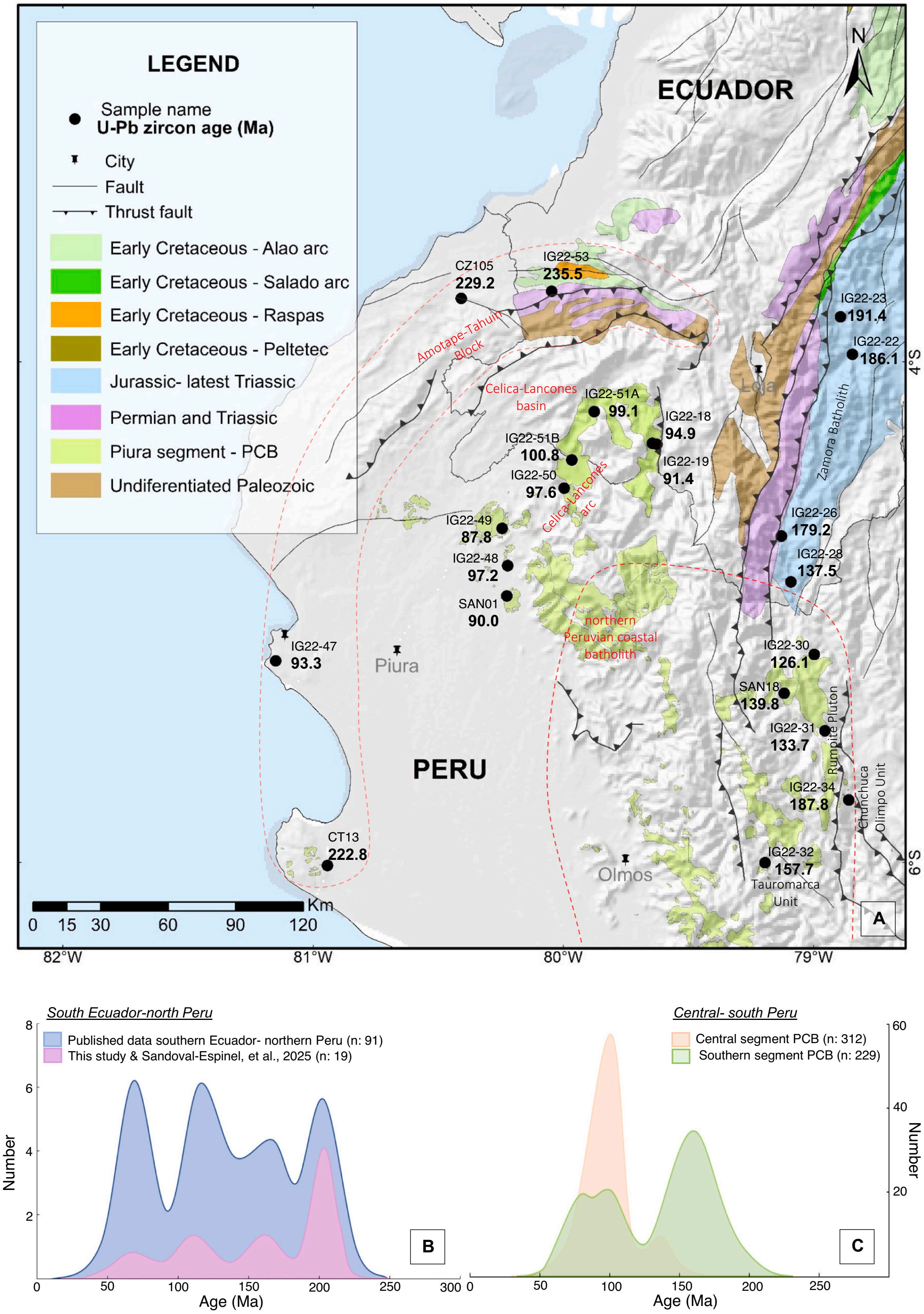

Fig. 3. (A) Map of the study area showing sample locations with their corresponding U—Pb zircon ages. The geological background includes Ordovician to Cretaceous units, while all Cenozoic units are shown in gray. (B) Age distribution functions for the geochronological data from the study area. (C) Age distribution functions for geochronological data from the central and southern segments of Peru, as reported by Martínez-Ardila et al. (2023). Only in situ rock data with ages between 66 and 250 Ma were included. Age spectra were generated using IsoplotR with a kernel bandwidth of 10 Ma for all graphs.

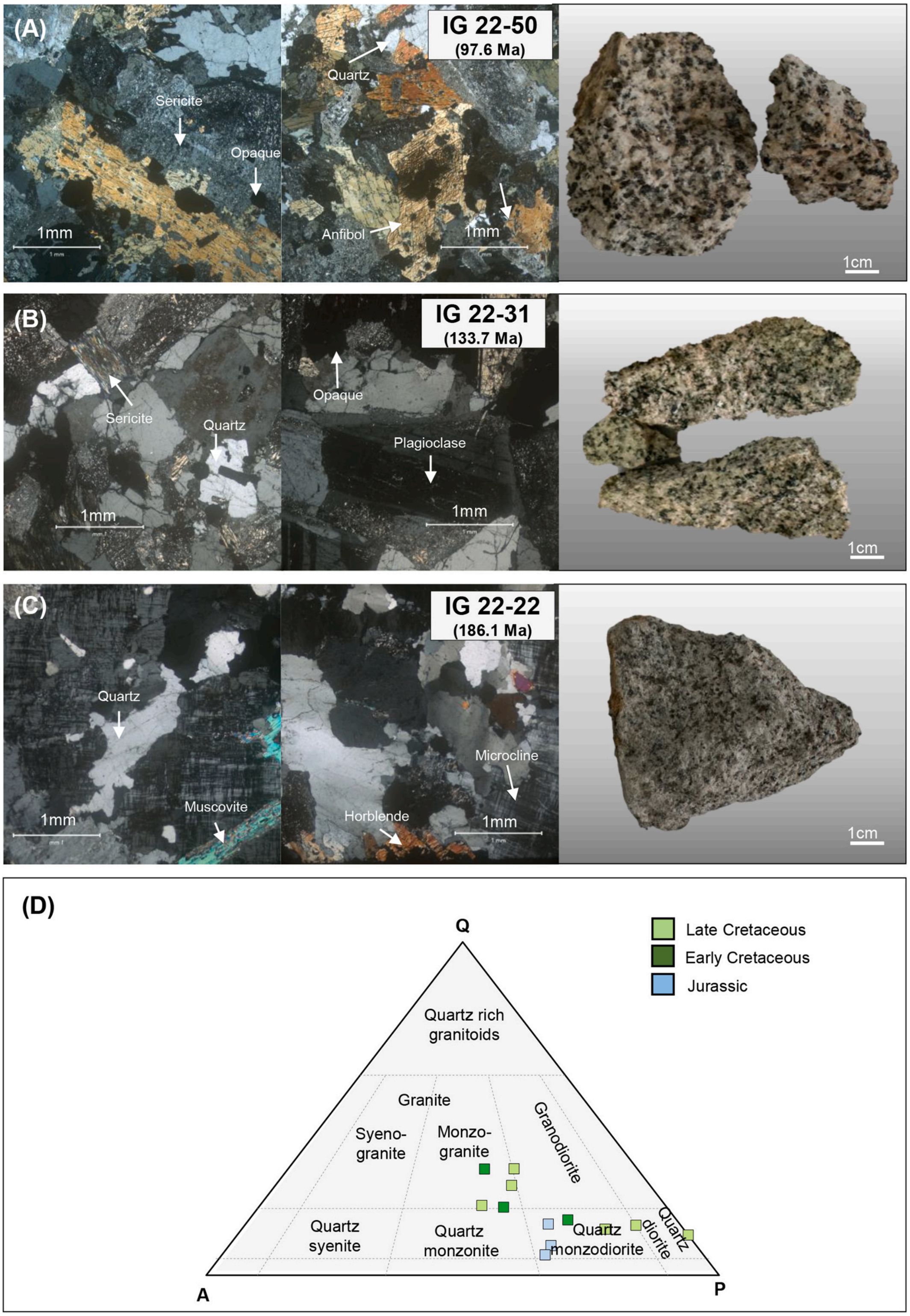

Fig. 4. (A-C) Photomicrographs of Mesozoic rocks displaying main mineral assemblages and Hand-size samples. (D) QAP diagram (Streckeisen, 1974) used to classify intrusive igneous rocks based on their mineralogy. Q, quartz. A, alkali feldspar. P, plagioclase.

Laboratory, University of Montpellier, France (AETE–ISO regional facility of the OSU OREME) using a ThermoFinnigan Neptune+ MC–ICP–MS (multicollector–inductively coupled plasma–mass spectrometer) coupled with a Photon-Machine Analyte G2 Excimer laser (193 nm wavelength); where ablation was performed using a 50 μm spot size, the laser frequency was 6 Hz and a fluence of 4.5 J/m^2. During the measurements, three zircon standards (91,500, GJ1 and Plešovice) with reference values taken from Blichert-Toft (2008); Morel et al. (2008); and Sláma et al. (2008); were treated as unknown in order to check the quality and the reproducibility of the data. All values were found to be in agreement with their references: 91,500 (^{176}Hf/^{177}Hf = 0.282305 ± 0.000020, n = 31), GJ1 (^{176}Hf/^{177}Hf = 0.282005 ± 0.000036, n = 23), and Plešovice (^{176}Hf/^{177}Hf = 0.282486 ± 0.00001, n = 21).

Hafnium isotopic data are expressed with the epsilon notation

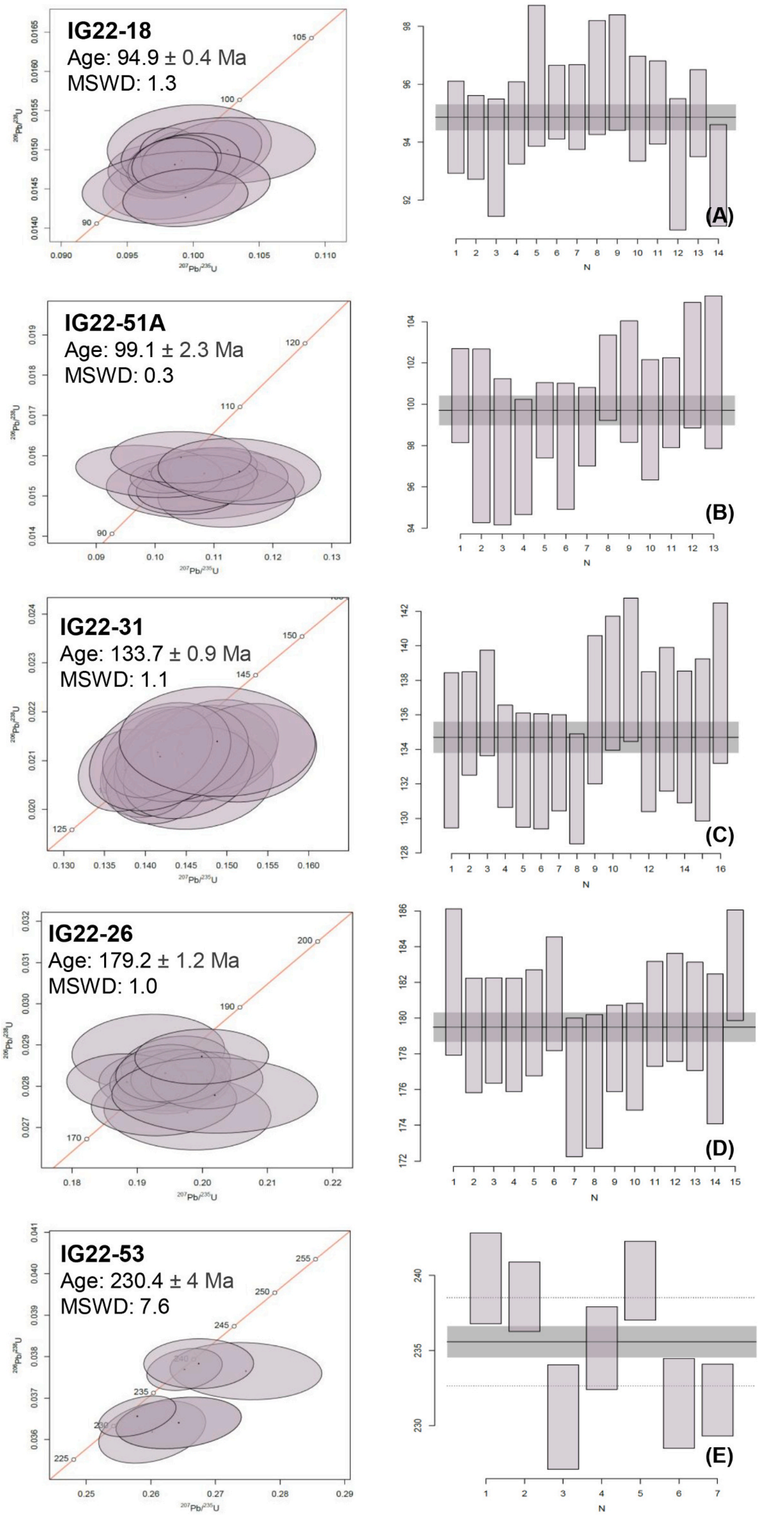

Fig. 5. Concordia (left) and weighted mean age (rigth) diagrams for selected samples, showing representative ages. Errors are expressed at 2σ. Plots were generated using ISOPLOT (Ludwig, 2003). (A) Sample IG22–18. (B) Sample IG22-51 A. (C) Sample IG22–31. (D) Sample IG22–26. (E) Sample IG22–53.

(εHf$_{(t)}$), representing the deviation of ^{176}Hf/^{177}Hf measured in a sample from the chondritic uniform reservoir (CHUR; Vervoort and Blichert-Toft, 1999), and presented in Table S9 within errors at 2 sigma level.

3.5. δ^{18}O analysis

Analysis of δ^{18}O in zircons are able to trace crust-mantle interaction through time and intracrustal recycling. This record is especially sensitive because oxygen isotope ratios of igneous rocks are highly affected by the incorporation of supracrustal materials into melts, which usually have δ^{18}O values higher than primitive mantle magmas (Valley et al., 2005).

Oxygen isotopic compositions in zircon were measured using a Cameca IMS 1270 E7 ion microprobe at the Centre de Recherches

Pétrographiques et Géochimiques (CRPG, CNRS), Université de Lorraine, Nancy (France) using a Cs + primary ion beam accelerated at 10 kV with an intensity of 2.5 nA. The detection mode was FC/FC (Faraday cup) multicollection. Instrumental mass fractionation from 4.41 ‰ to 6.418 ‰ using BrF5 extraction and a gas source mass spectrometer.

Measured $^{18}O/^{16}O$ ratios were normalized using Vienna Standard Mean Ocean Water compositions (VSMOW, $^{18}O/^{16}O = 0.0020052$; Gonfiantini et al., 1995), then corrected for the instrumental mass fractionation factor (IMF), and reported within 1 sigma error (Table S10); further technical information can be found in Witt et al. (2023).

3.6. Trace elements analysis in Zircon

Zircon is a robust mineral known for its capacity to incorporate trace elements into its crystal lattice (Belousova et al., 2002; Grimes et al., 2007). This mineral demonstrates a remarkable resistance to chemical alteration, making it a powerful geochemical tracer for studying geological processes (Belousova et al., 2002). Rare Earth Elements found in zircons can provide insights into the conditions during which zircon crystallized, revealing information about the composition of parental magmas (Grimes et al., 2007; and references therein).

Zircon trace-element concentrations were measured at Géosciences Montpellier (University of Montpellier, AETE-ISO regional facility of the OSU OREME) using LA-ICP-MS, whose analytical platform includes a 193 nm ArF excimer laser (Teledyne G2) coupled to a Thermofinnigan Element XR mass spectrometer modified by the addition of an 80 m^3/h Edwards primary pump in the interface to enhance sensitivity. The laser was operated at a repetition rate of 6 Hz, using a 50 μm spot size and a fluence of 4.5 J/m^2. The total analysis time was 120 s with the first 80 s used for background measurement prior to sample ablation. NIST 612 was used for external calibration with reference values from Pearce et al. (2007). The accuracy and long-term reproducibility of the measurements were ensured by analyzing three zircon standards (91,500 $n = 20$; GJ1 $n = 11$ and Plešovice n = 11). Finally, data reduction was carried out with the software package Glitter (van Achterberg et al., 2001), and is presented in Table S11.

Data was further filtered to exclude measurements that may have been influenced by the presence of inclusions, following the criteria proposed by Attia et al. (2020), which involve excluding analyses with high counts of Y (>5000 ppm), and LREE ([Ce] > 200 ppm; [Sm] > 300 ppm; [Eu] > 15 ppm and [Gd] > 150 ppm).

4. Results

4.1. Petrographic analyses

Twelve thin sections from monzogranite, quartz diorite, and quartz-monzodiorite samples were examined for petrographic characterization (Table S3). All samples displayed phaneritic textures (Figs. 4 and S3), with crystal sizes ranging from 0.8 to 2.7 mm (Fig. 4). The primary mineral assemblage was composed of quartz, orthoclase, microcline, plagioclase, muscovite, and biotite phenocrysts, accompanied by minor amounts of hornblende, apatite, and opaque minerals. The rocks are relatively pristine, with well-preserved grain boundaries and limited evidence of alteration. This is supported by their loss on ignition (LOI) values, which range from 0.85 to 1.94 (Table S8). However, minor plagioclase sericitization and slight biotite chloritization were observed locally.

The rocks are predominantly felsic in composition. Jurassic samples plot in the quartz monzodiorite field, while Early Cretaceous rocks fell into the monzogranite and quartz monzodiorite fields. In contrast, Late Cretaceous rocks exhibited a wider compositional range, with samples falling into the quartz diorite, quartz monzodiorite, and monzogranite fields (Fig. 4D; The geochronological framework for these age groups is presented in Section 4.2).

4.2. Zircon U—Pb geochronology

Nineteen new zircon U—Pb ages were obtained in this study, supplemented by two previously published Triassic ages from Sandoval-Espinel et al. (2025): samples CT013 (222.8 ± 1.2 Ma) and CZ105 (229.2 ± 1.4 Ma).

Sample IG22–53 (Fig. 5E) clearly exhibits two distinct age populations. Given the magmatic nature of the rock, the best estimate for its maximum crystallization age was based on the youngest coherent population ($n = 3$), yielding a weighted mean age of 230.4 ± 4 Ma.

The Mesozoic ages obtained in this study were distributed as follows: i) one Triassic sample (230.4 ± 4) from the ATB; ii) five Jurassic samples from the eastern Ecuadorian and western Peruvian Cordilleras, with ages ranging from 191.4 ± 5.3 Ma (IG22–23) to 157.7 ± 4.2 Ma (IG22–32); iii) four Early Cretaceous samples (also from the Cordilleras), with ages ranging from 139.8 ± 1.8 Ma (SAN18) to 126.1 ± 3.6 Ma (IG22–30); and iv) nine Late Cretaceous samples from the Celica–Lancones arc, ranging from 100.8 ± 1.8 Ma (IG22-51B) to 87.8 ± 1.7 Ma (IG22–49).

4.3. Whole rock geochemistry

Fifteen samples were selected for whole-rock geochemical analysis (Table S8). Only one Triassic sample was analyzed in this study due to the extensive geochemical data available in the literature for this period (e.g., Cochrane et al., 2014; Mišković et al., 2009). In the total alkali versus silica (TAS) classification scheme (Fig. 6A), Triassic samples—both published data and those analyzed in this study—plot within the granite, granodiorite, and quartz monzonite fields. Jurassic samples fall predominantly within the granodiorite field, while Early Cretaceous samples are classified as granite, granodiorite, and quartz monzonite. In contrast, Late Cretaceous samples exhibit greater compositional diversity, ranging from granites and granodiorites to diorites and gabbros. In general, most samples analyzed were felsic in composition, with only a few exhibiting intermediate to mafic characteristics.

In general, the felsic rocks possessed compositions that ranged between 63.4 and 75.1 wt% SiO_2, 13.5–17.1 wt% Al_2O_3, 0.24–3.9 wt% MgO, and 0.62–7.98 wt% CaO, while the intermediate to mafic rocks possessed composition ranges between 49.1 and 59.9 wt% SiO_2, 18.1–19.5 wt% Al_2O_3, 1.7–7.8 wt% MgO, and 7.2–14.1 wt% CaO (all values recalculated to an anhydrous basis; Table S8).

The La/Yb and Sr/Y ratios, which are commonly used as proxies for crustal thickness (Chapman et al., 2015; Profeta et al., 2015), show a consistent trend from the Triassic to the Cretaceous (Fig. 7).

4.4. Zircon isotopic data

A total of 130 $\varepsilon Hf_{(t)}$ analyses are presented in Table S9, with results illustrated in Fig. 8A. The $\varepsilon Hf_{(t)}$ values in the Triassic samples range between −12.8 and 1.2, while the Jurassic samples range between 4.5 and 7.5, with an outlier at −17.8. Early Cretaceous $\varepsilon Hf_{(t)}$ values vary from 4.4 to 11.8, while samples from the Late Cretaceous exhibit the highest $\varepsilon Hf_{(t)}$ values, fluctuating between 8.5 and 14.8, with three outliers at −10.1, −1.9, and 3.1. In general, the $\varepsilon Hf_{(t)}$ values are indicative of long-term depletion from about 200 to about 85 Ma (Fig. 8A). It should be note that the samples reach their maximum values in the Late Cretaceous (~100 Ma), with values approaching depleted mantle signatures before slightly decreasing toward ca. 85 Ma, although this trend is subtle.

A total of 44 $\delta^{18}O$ measurements are reported in Table S10, with results illustrated in Fig. 8B. The $\delta^{18}O$ values for the Triassic samples show supracrustal signatures ranging from 8.3 to 11 ‰, with an outlier at 4.7 ‰. Samples from the Jurassic exhibit relatively uniform $\delta^{18}O$ values (5.3–6.2 ‰), which are close to mantellic compositions, with one higher outlier at 9.5 ‰. Early Cretaceous $\delta^{18}O$ values range between 3.9 and 6.5 ‰, while Late Cretaceous samples exhibit ranges from 3.3 to 5

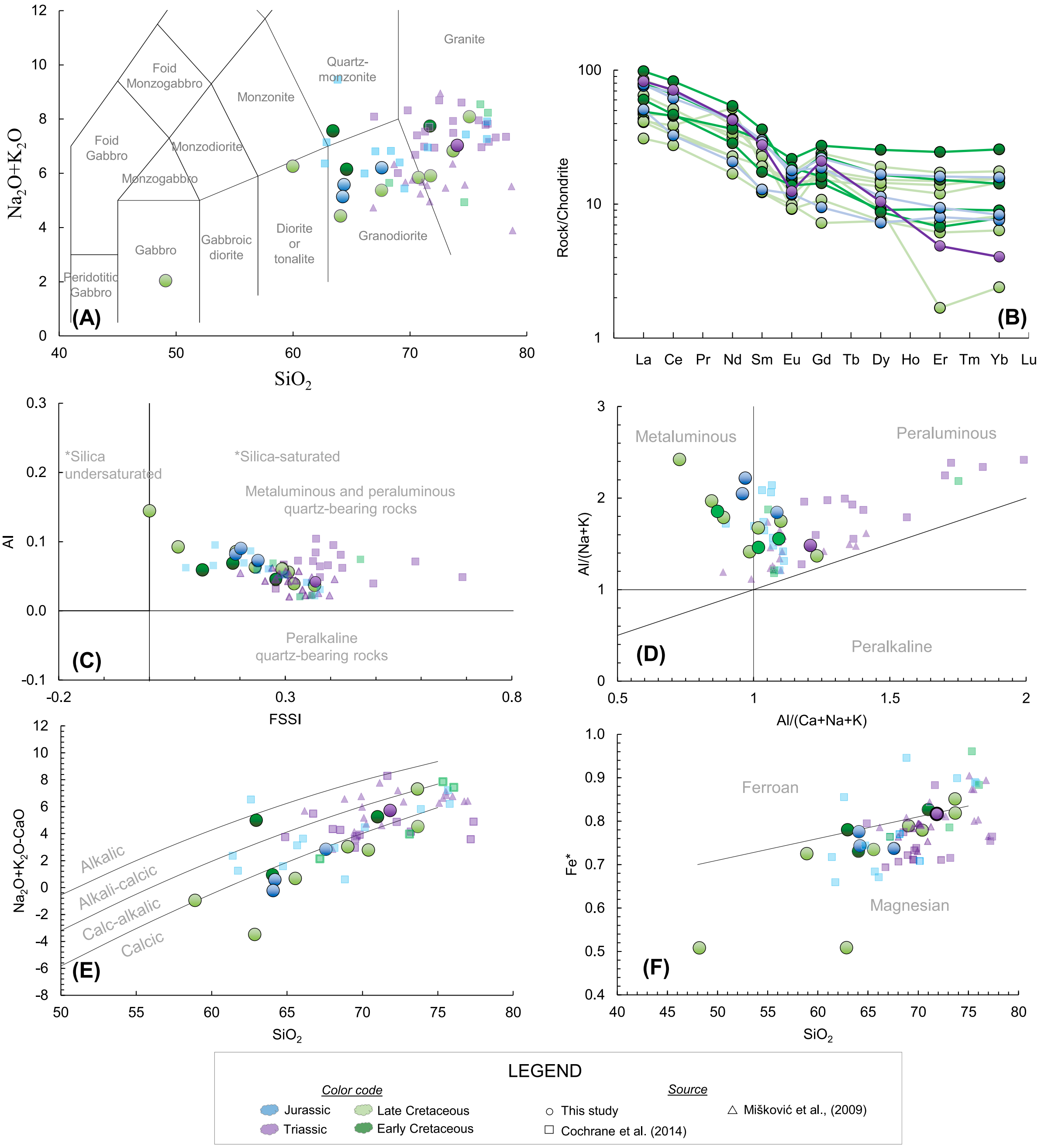

Fig. 6. Whole rock classification diagrams. (A) Total alkali versus silica plot (Middlemost, 1994). (B) Chondrite-normalized rare element plot, normalizing values are from Sun and McDonough (1989). (C) Plot of alkalinity index (AI) vs feldspathoid silica-saturation index (FSSI). (D) Molar A/CNK versus molar A/NK plot. (E) $Na_2O + K_2O$-CaO as a function of SiO_2, fields are from Frost and Frost, 2008. (F) Fe* versus SiO2 plot (Frost et al. 2001).

‰, with two outliers exceeding 7 ‰. There is a clear decrease in $\delta^{18}O$ values over time, with values trending toward mantle-like signatures (Fig. 8B).

4.5. *Zircon geochemistry*

The zircon geochemical dataset comprises 121 measurements that exhibit considerable variability in several trace elements, including Dy (25–864 ppm), Gd (3–231 ppm), U (42–8130 ppm), and Y (285–9140 ppm) (Table S11). The chondrite-normalized trace element patterns exhibited trends that were typical of continental arc samples (Fig. 9A; Hoskin and Schaltegger, 2003) with significant enrichment in HREE relative to LREE $(Yb/Sm)_{CN} = 44–118$; $(Yb/Gd)_{CN} = 13–39$) and negative Eu anomalies (Eu/Eu* = 0.20–0.31).

The zircons exhibited Th/U ratios ranging from 0.03 to 2.5 (Fig. 9B), indicative of magmatic origins. However, some crystals from the Triassic exhibited low Th/U values (0.03–0.06), which can be indicative of metamorphic environments (Th/U $<$ 0.1; Grimes et al., 2007). The majority of zircon grains are derived from felsic rocks (Th/U $>$ 0.1; Grimes et al., 2015; Teipel et al., 2004), with the exception of some Early Cretaceous crystals that suggest a more mafic source (Th/U = 1.9–2.5). In addition, most of the zircon grains possess characteristics that are consistent with continental arc formation, while a subset of the Late Cretaceous grains exhibit signatures that are consistent with a mid-ocean ridge environment (Fig. 9C and Fig. 9D).

The Triassic zircon crystals exhibit S-type to “hybrid” S-type signatures although a few plot in the I types, based on the classification scheme proposed by Roberts et al. (2024); these are consistent with the

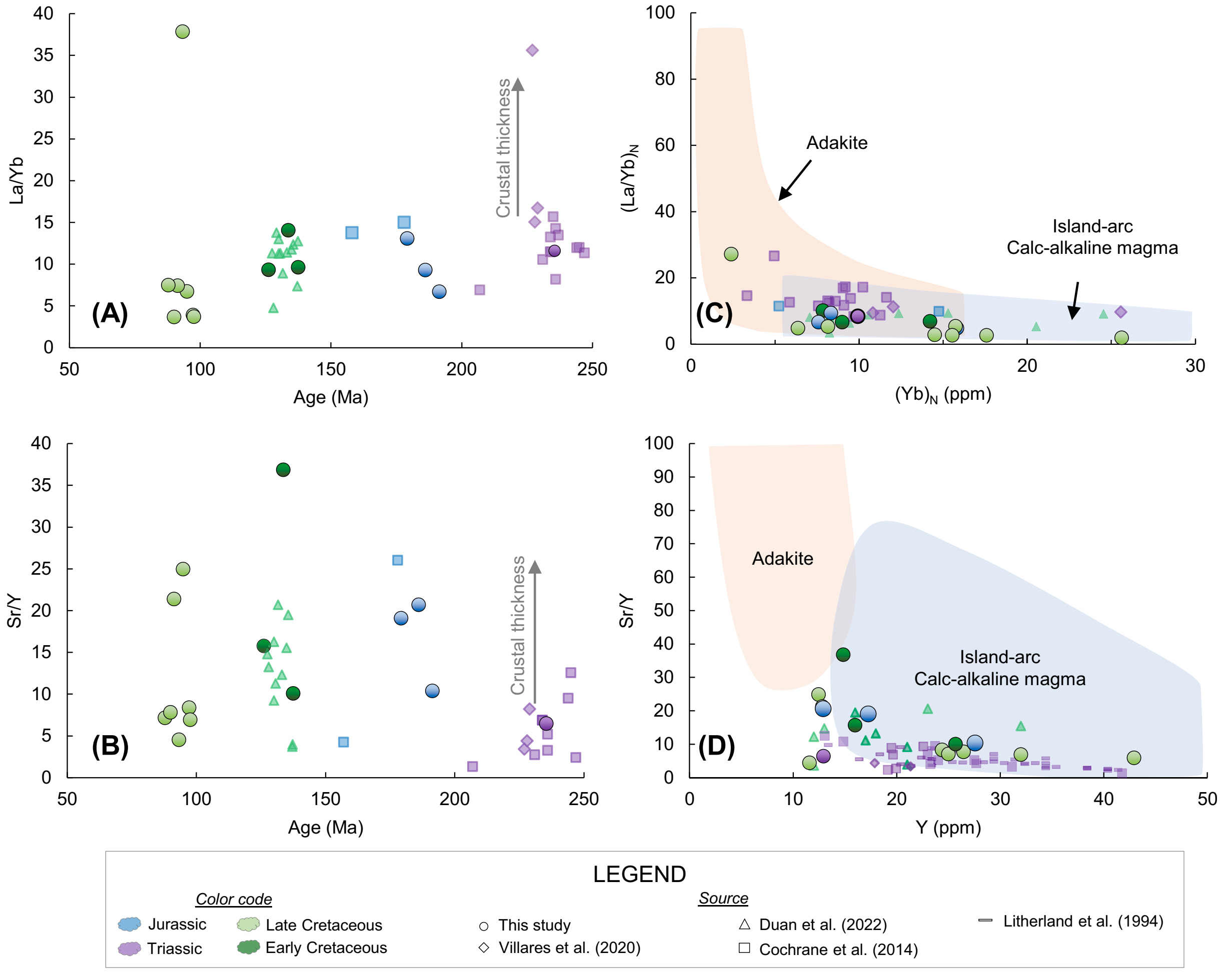

Fig. 7. Whole-rock petrogenetic proxies related to crustal thickness and adakite discrimination diagrams. (A) La/Yb vs. Age. (B) Sr/Y vs. Age. (C) $(La/Yb)_N$ vs. Yb_N (after Martin, 1986; N = chondrite-normalized). (D) Sr/Y vs. Y (after Drummond & Defant, 1990).

findings of Aspen et al. (1992) and Riel et al. (2014). In contrast, the Jurassic and Late Cretaceous zircon grains exhibit signatures typical of I-type granitoids (Fig. 9E), while Early Cretaceous grains possess features that are characteristic of both I-type and S-type granitoids.

U/Yb ratios are used to distinguish continental and oceanic zircons and assess crustal contributions in magmas, as this ratio often reflects depletion or enrichment as well as the extent of crustal assimilation (Grimes et al., 2007; Grimes et al., 2015). There was a gradual increase in U/Yb ratios from the Triassic to the Early Cretaceous, indicative of progressive enrichment (Fig. 10A). However, this trend was disrupted in the Late Cretaceous, where zircons exhibit both high and low U/Yb values, indicating that they were derived from a mixed source. Notably, the high observed Th/U values were primarily associated with sample IG22–19, which also exhibits anomalously high U concentrations. It should be noted that IG22–19 was the most inland sample of the Late Cretaceous group.

Ratios such as Yb/Gd, Nb/Ta, and LREE/HREE can be used as indicators of melting depth, as they reflect pressure-dependent mineral fractionation in key mineral phases (e.g., garnet, amphibole, clinopyroxene, and plagioclase). Consequently, they are often used as proxies for crustal thickness (Drabon et al., 2024; Grimes et al., 2015). There is a progressive increase in Nb/Ta, LREE/HREE, and Eu/Eu ratios from the Triassic to the Early–Middle Cretaceous, though this trend is less evident in Late Cretaceous zircon grains. Dy/Yb decreases over the same interval, while Yb/Gd exhibits no distinct trends (Fig. 10).

5. Discussion

5.1. Triassic crustal reworking

Triassic magmatism, recorded between 247.2 ± 4.3 Ma and 203 ± 1.4 Ma, is associated with the Moromoro, Sabanilla, and Tres Lagunas units along the western flank of the Ecuadorian Eastern Cordillera as well as the Marcabelí, La Victoria, and La Florida granitoids of the ATB (e.g., Cochrane et al., 2014; Feininger & Silberman, 1982; Litherland, 1994; Sandoval-Espinel et al., 2025). Triassic magmatism has also been identified further east in the Chinchiná unit, located at ~75.5°W (e.g., Cochrane et al., 2014; Litherland, 1994; Table S1), indicative of the existence of a broad magmatic arc. The U—Pb zircon data presented in this study support and refine these observations, with documented crystallization ages ranging from 230.4 ± 4 to 222.8 ± 1.2 Ma, which are consistent with previous ages reported for the ATB (Figs. 2, 3 and 11).

Triassic magmatism along the western margin of the Northern Andes is attributed to mantle upwelling resulting from lithospheric thinning and extension, processes interpreted to result from either continental rifting during Pangea fragmentation or changes in subduction dynamics (e.g., Riel et al., 2018; Spikings et al., 2015; Villares et al., 2020). Our dataset refines these interpretations by constraining the degree and timing of crustal involvement during this magmatic episode. The Triassic granitoids investigated in this study exhibit strong crustal assimilation as shown by high $\delta^{18}O$ values (up to 11 ‰) and low $\varepsilon Hf_{(t)}$ values (−12 to +2), indicating that prolonged crustal reworking

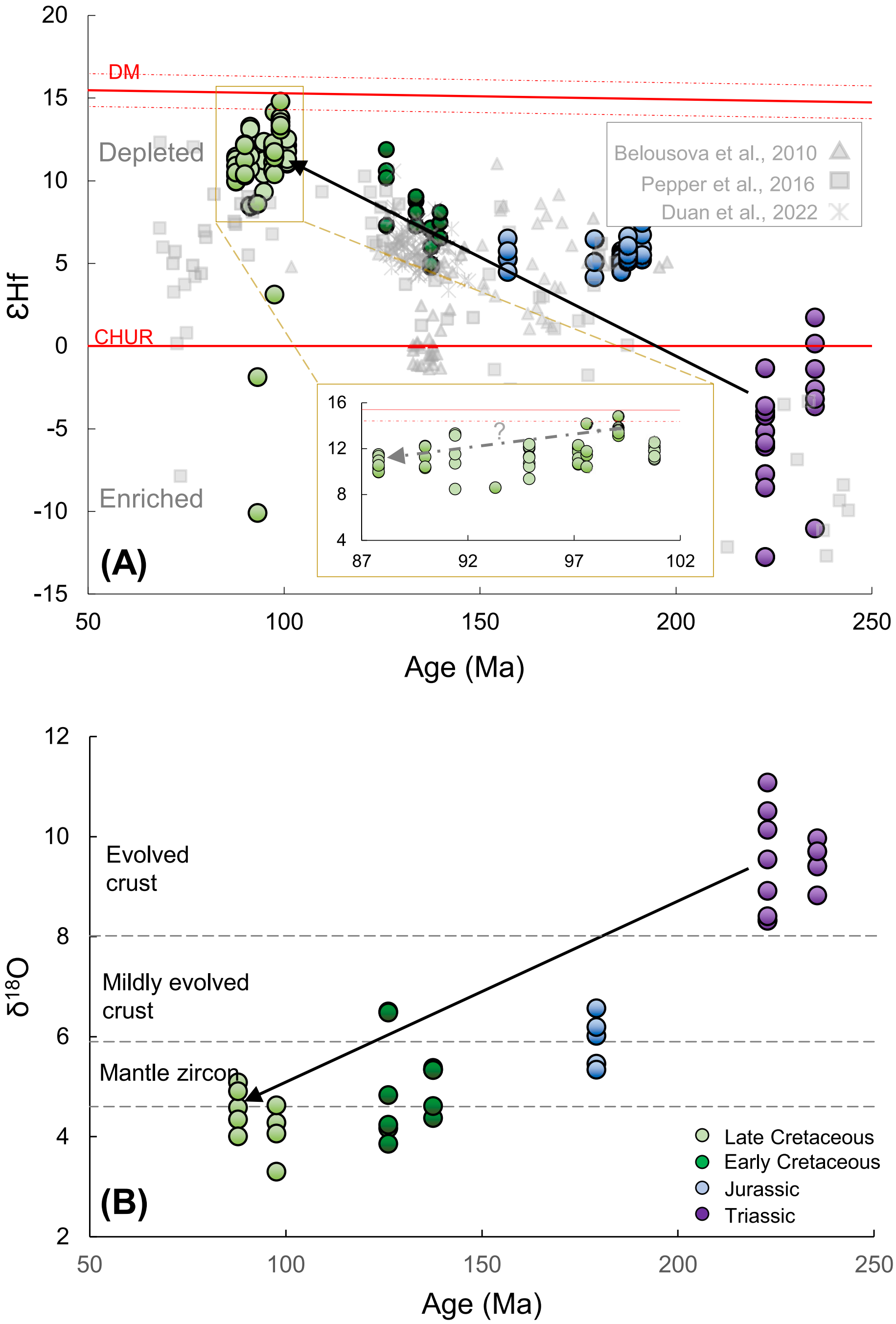

Fig. 8. Isotopic data for the study area. (A) εHf vs. Age, including published εHf isotopic data from detrital zircons by Belousova et al. (2010) and Pepper et al. (2016). (B) $\delta^{18}O$ vs. Age. Limits are from Valley et al. (2005).

persisted until at least ~220 Ma (Fig. 8). This is consistent with models proposed by Riel et al. (2018) and Villares et al. (2020), which documented S- and A-type magmatism along the western Gondwana margin during the same period. Our dataset also reveals a trend from S-type to hybrid S-type, and to I-type granites signature (235–222 Ma; Fig. 9E), emphasizing the significant contribution of supracrustal materials to magmatic reservoirs and providing further evidence of extensive crustal reworking.

The Triassic granitoids exhibit magnesian and calc-alkalic geochemical signatures (Fig. 6E and F) that are characteristic of arc environments (Frost and Frost, 2023; and references therein). The high Dy/Yb (Fig. 10B) and low Yb/Gd (Fig. 10C) ratios in the Triassic zircons are indicative of garnet stability in the source residue, consistent with deep crustal melting in a thickened crust (Drabon et al., 2024; and references therein). Some Triassic samples also display elevated whole-rock La/Yb ratios (Fig. 7A and C), which are compatible with magma derivation from a thick crust. In contrast, whole-rock Sr/Y ratios (Fig. 7B and D) do not show high values typically interpreted as evidence of crustal thickening. Recent studies, however, have shown that crustal thickness estimates based on Sr/Y can deviate substantially from geophysically determined values due to the strong influence of fractionation processes (Guo and Yang, 2023). Consequently, we suggest that Triassic magmatism was generated in an active subduction setting through partial melting and reworking of a previously thickened continental crust (Fig. 12A).

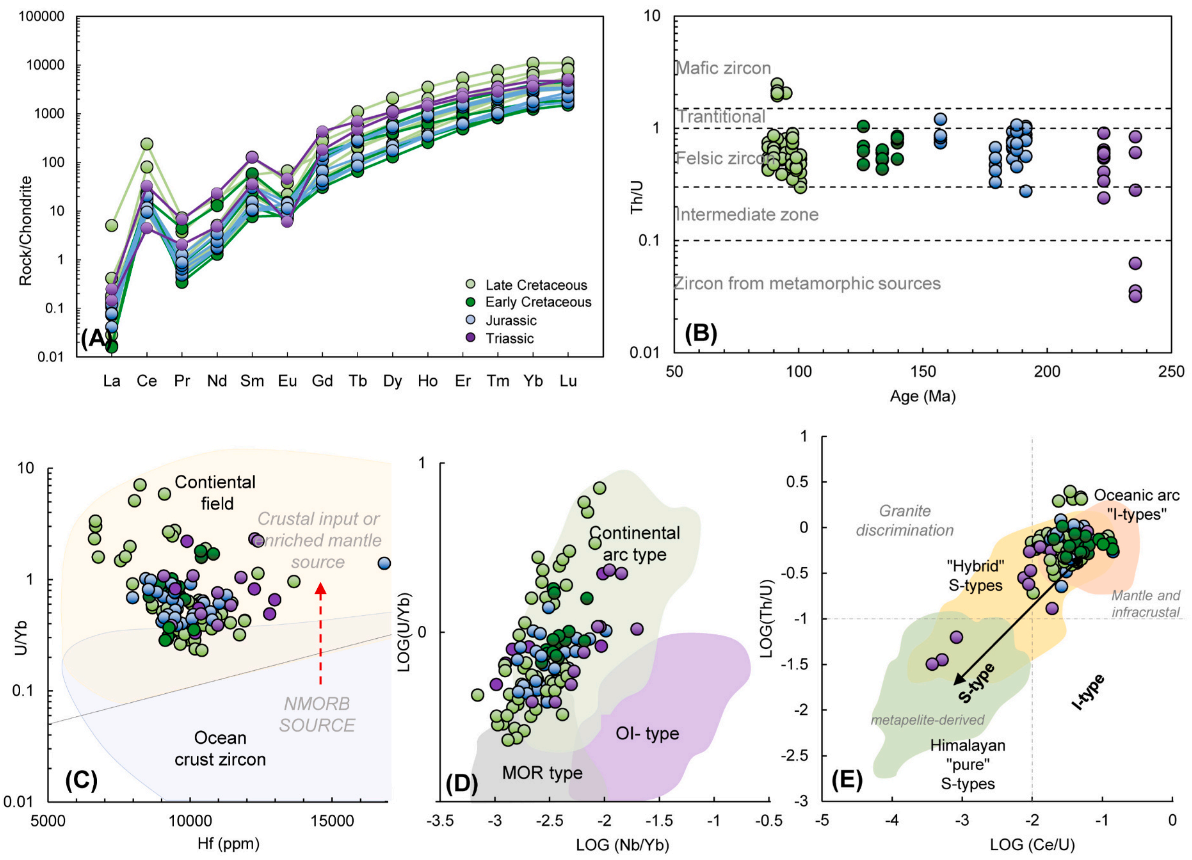

Fig. 9. Zircon-based classification diagrams. (A) Chondrite-normalized rare element plot, normalizing values are from Sun and McDonough (1989). (B) Th/U versus age plot. (C) U/Yb vs Hf, fields for continental and oceanic zircon are from Grimes et al. (2007) (D). Tectonic discrimination diagram, boundaries are from Grimes et al. (2015). (E) Th/U vs Ce/U plot defining I-type, S-type and hybrid S-type granitoids, boundaries are from Roberts et al. (2024). MOR: Mid ocean ridge. OI: ocean island.

5.2. *Jurassic magmatism: From strong crustal reworking to predominantly mantle inputs*

Jurassic magmatic activity in northwestern South America is recorded by Lower–Middle Jurassic batholiths in Colombia and by the Abitagua and Zamora batholiths in Ecuador (Fig. 2; Bayona et al., 2020; Bustamante et al., 2016; Cochrane et al., 2014; Leal-Mejía et al., 2019; Spikings et al., 2015).

In southern Ecuador, specifically, Jurassic magmatism is primarily represented by the Zamora Batholith. The crystallization ages for the batholith have been constrained by various geochronological techniques, including K—Ar dating on hornblendes and biotites (201–151 Ma; Gendall et al., 2000; Litherland, 1994), U—Pb dating on zircons (180–145 Ma; Chiaradia et al., 2009; Cochrane et al., 2014; Drobe et al., 2013), and ^{40}Ar—^{39}Ar dating on hornblendes (160–150 Ma; Chiaradia et al., 2009; Coder, 2003). The U—Pb zircon ages presented in this study range from 191 ± 5 Ma to 157 ± 4.2 Ma, extending the previously known magmatic interval and suggesting that the onset of Jurassic magmatism occurred significantly earlier than previously reported. Our data also provide the first direct evidence of Jurassic magmatism in northern Peru, with samples IG22–32 and IG22–34 yielding crystallization ages of 157.7 ± 4.2 Ma and 187.8 ± 3.2 Ma, respectively. These results show that the Jurassic magmatic arc extended further south into northern Peru, at least as far as 6°S, indicating that Jurassic magmatic activity was more widespread than previously recognized.

Furthermore, samples IG22–22, IG22–23, IG22–26, and IG22–34 have Early Jurassic crystallization ages ranging from ca. 191 to 179 Ma, overlapping with the crystallization ages of the Norosí and San Martín batholiths (189–182 Ma) as well as the Mocoa-Garzón batholith (180–172 Ma) in Colombia (e.g., Leal-Mejía et al., 2019; and references therein). These results call for a re-evaluation of the southward-younging model of magmatism proposed by Spikings et al. (2015), which was based on data available at that time.

Jurassic isotope data reveal intermediate εHf$_{(t)}$ values (4.2–7.5; Fig. 8A) and a shift from >8 ‰ to 5.3–6.5 ‰ δ^{18}O values (Fig. 8B). This trend indicates a transition toward more juvenile compositions as well as increasing mantle contribution over time. Jurassic magmatism exhibits a compositional change from peraluminous to metaluminous (Fig. 6C and D) as well as magnesian and calcic geochemical signatures (Fig. 6E and F) indicative of less evolved magma sources (e.g., Frost and Frost, 2008). This geochemical evolution is also expressed as a shift from S-type to I-type granitoids (Fig. 9E), accompanied by decreasing Dy/Yb zircon ratios (Fig. 10B and F), indicating melting in a garnet-free, plagioclase-stable source at relatively shallow crustal levels (Drabon et al., 2024; Grimes et al., 2015). We interpret Jurassic magmatism (191 ± 5 Ma to 157 ± 4.2 Ma) as the product of lithospheric thinning associated with intra-arc extension, which facilitated mantle-derived magmatism with limited crustal recycling (Fig. 12B). Furthermore, our data do not support a thick Jurassic crust (190–180 Ma) proposed by Chavarría et al. (2022), given the geochemical evidence for crustal thinning and shallow-level melting.

Jurassic extensional tectonics have already been documented in the Northern Andes (e.g., Bustamante et al., 2016; Cochrane et al., 2014; Spikings et al., 2015). For instance, Spikings et al. (2015) and Cochrane et al. (2014) investigated Jurassic magmatism in the Ecuadorian Andes and suggested that, based on older arc-related rocks dated between 209

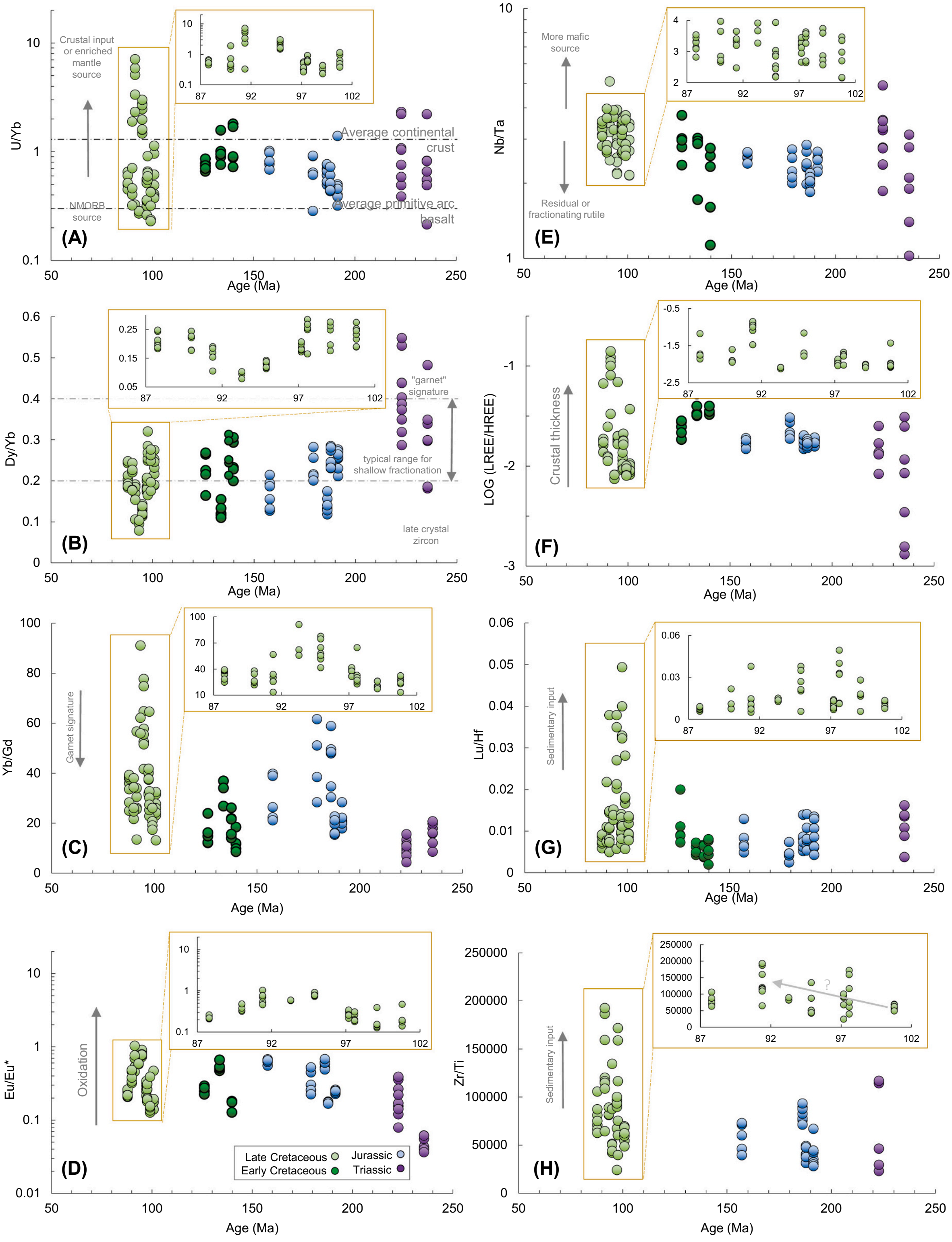

Fig. 10. Zircon bivariate plots showing various proxies. (A) Age vs. U/Yb as a proxy for melt maturity, with domains from Grimes et al. (2015). (B—F) plots of proxies for crustal thickness, including (B) Dy/Yb vs. Age, (C) Yb/Gd vs. Age, (D) Eu/Eu* vs. Age. (E) Nb/Ta vs. Age, and (F) LREE/HREE vs. Age. (G-H) plots of proxies for sediment input, including (G) Lu/Hf vs. Age, and (H) Zr/Ti vs. Age.

and 194 Ma in the Santander Massif of Colombia, the arc axis migrated oceanward between 194 and 189 Ma (Van der Lelij, 2013). Slab rollback induced a westward arc migration from the Cordillera Real to the Western Cordillera (Fig. 1), resulting in the emplacement and development of a long-lived magmatic arc that persisted until ~140 Ma. This arc migration is attributed to crustal extension above a retreating subduction zone, leading to the progressively reduced continental contamination of mantle-derived magmas. While we agree with an

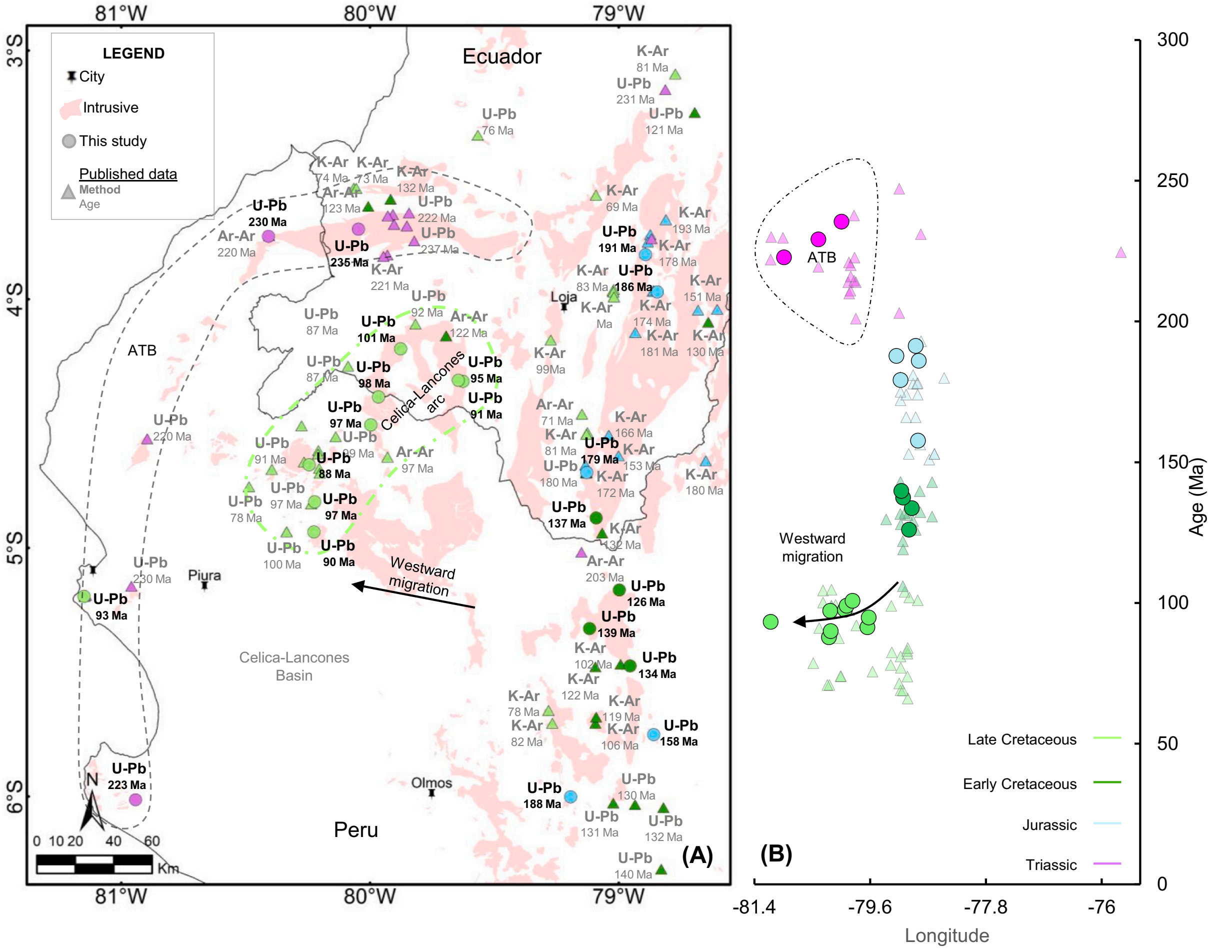

Fig. 11. (A) Sketch of the area showing arc position during Mesozoic. (B) Latitude vs age of the Mesozoic samples.

overall decrease in crustal input, our U—Pb zircon ages do not support such an early timing for arc migration (see Section 5.3).

The petrological characterization of Jurassic magmatism in the Colombian Andes by Bustamante et al. (2016) concluded that oblique convergence of the Farallon Plate (~170–130 Ma) limited the incorporation of fusible sediments into the mantle, resulting in a more refractory mantle with a primitive isotopic signature, consistent with the isotopic signatures observed in this study (Fig. 8). This allow us to suggest that, during the Jurassic, the southernmost Northern Andes was subject to similar geodynamic conditions and mantle source characteristics as the Colombian Andes.

5.3. *Early–Middle cretaceous dynamics: Westward magmatic migration and the evolution of the Celica-Lancones basin*

Early Cretaceous magmatism in the Peruvian Western Cordillera has primarily been dated by whole-rock K—Ar, yielding ages ranging from 122 ± 6 Ma to 102 ± 5 Ma (Hama, 1990), while limited U—Pb dating in the region reveals ages ranging from 140 Ma to 130 Ma (CGS_INGEMMET, 2017). Similarly, Early Cretaceous magmatism in southern Ecuador has primarily been constrained by whole-rock K—Ar dating (119 ± 6 to 106 ± 5 Ma; Hama, 1990), ^{40}Ar/^{39}Ar dating on hornblende (126 ± 4 to 122 ± 1 Ma; Urlich, 2005), and a few U—Pb zircon ages ranging from 131 ± 1 Ma to 104 ± 2 Ma (Cochrane, 2013; Winter, 2008). Our study supplements this information with new U—Pb zircon ages ranging from 140 ± 2 Ma to 126 ± 4 Ma.

Early Cretaceous magmatism coincided with a major change in subduction direction from WSW to NNE around 145–140 Ma (Riel et al., 2014), followed by basal accretion of the Raspas Ophiolitic Complex between 130 and 120 Ma (Gabriele, 2002; Riel et al., 2014). During this process, oceanic lithosphere (MORB crust ± seamount/oceanic plateau fragments) was subducted, metamorphosed at high pressure, and subsequently underplated to the lower crust before being exhumed in the ATB during the Late Cretaceous (Riel et al., 2014; and references therein).

Early Cretaceous magmatic reservoirs (140–126 Ma) are characterized by zircon δ^{18}O values within and near the mantle array and mid-enriched to depleted $\varepsilon Hf_{(t)}$ values (+4.4 to +11.8), indicating a predominantly mantle-derived source. Additionally, their trace-element compositions, including low Dy/Yb ratios, elevated LREE/HREE ratios, and low Yb/Gd values (Fig. 10), suggest that differentiation occurred under upper amphibolite-facies conditions (Drabon et al., 2024; and references therein). We suggest that the Early Cretaceous magmatism developed in an extensional subduction setting, where progressive crustal thinning enhanced the influx of mantle-derived melts into the magmatic system. A minor contribution from the underplated oceanic materials at the base of the crust remains possible and cannot be excluded (Fig. 12C; Riel et al., 2014). The proposed extensional regime is reflected in the regional stratigraphy, with a widespread Early Cretaceous angular unconformity as well as the development of deep sedimentary basins such as the Chicama Basin in northern Peru (Jaillard and Soler, 1996), and the Celica-Lancones in southern Ecuador north Peru (Jaillard et al., 1999).

Intrusive bodies dated between 100 and 88 Ma are systematically located to the west of intrusions dated as late as ~126 Ma (see former section). This distribution supports the interpretation of a westward

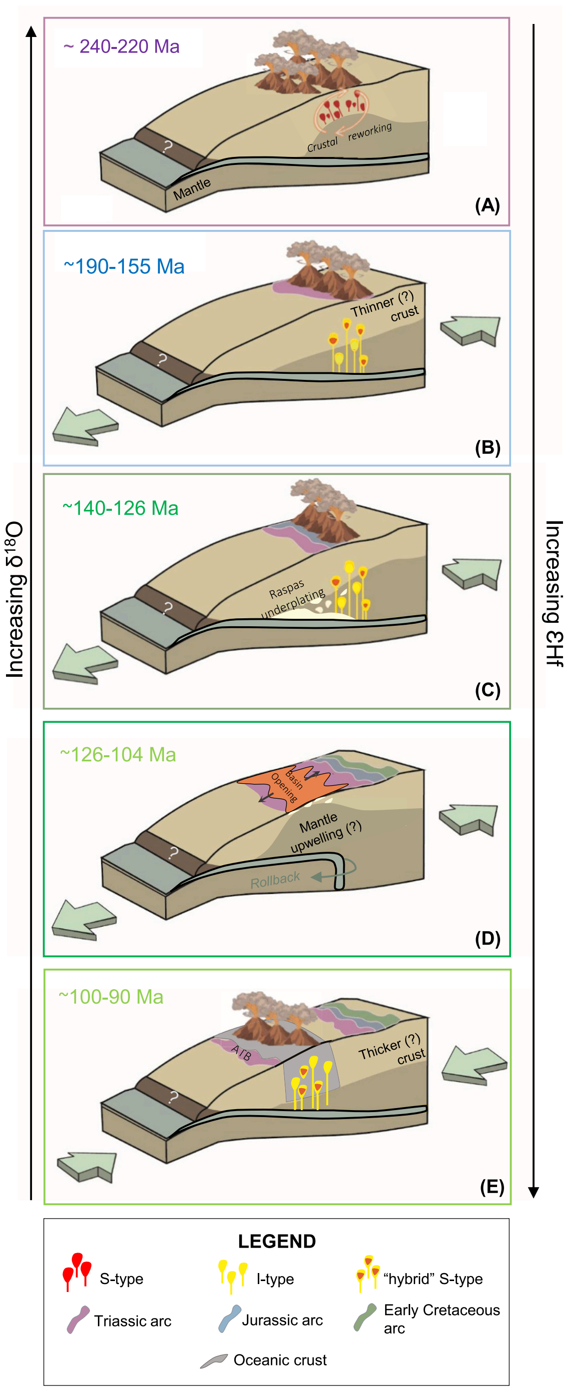

Fig. 12. Generalized time-slice sketches illustrating the Mesozoic tectono-magmatic evolution of southern Ecuador and northern Peru, as constrained by this study. (A) 240–220 Ma: arc magmatism and crustal reworking; (B) 190–155 Ma: extensional arc development; (C) 140–126 Ma: subduction of oceanic Raspas complex and underplating to the lower crust; (D) 126–104 Ma: rollback and opening of the Celica–Lancones basin; (E) 100–90 Ma: onset of compression and establishment of a new western arc emplaced on oceanic crust.

migration of magmatism during the Middle to Late Cretaceous. We constrain the younger limit of this migration to ~104 Ma based on the oldest age reported by Winter et al. (2010) in the Celica–Lancones arc, located to the east. The westward shift marks the relocation of a previously stationary arc set at ~79°W (present-day coordinates) that was active between ~190 and ~ 126 Ma (Fig. 11). This migration is coeval with the opening of the NE–SW trending Celica–Lancones Basin (~110–100 Ma; Fig. 12D; Jaillard et al., 1999; Mourier, 1988; Winter, 2008). During this rifting setting, the ATB block detached from the South American margin and underwent a ~ 65° clockwise rotation (Mourier, 1988; Riel et al., 2014).

Given the accentuated extensional deformation in the basin, and considering the relatively old age of the subducting slab (~60 Ma; Maloney et al., 2013), we propose that slab rollback, occurring at the same time as the formation of the Celica–Lancones Basin around 110 Ma, was the main cause of arc migration. Rollback-related processes likely also contributed to within-plate alkaline magmatism (110–82 Ma) in the Ecuadorian Oriente Basin, consistent with our interpretation (Barragán et al., 2005).

A westward arc migration has also been documented in Colombia, Ecuador, and northern Peru (Cochrane et al., 2014; Duan et al., 2022; Leal-Mejía et al., 2019; Ramos, 2009; Spikings et al., 2015). Some studies suggest that this magmatic shift began in northern Peru at around ~145 Ma (Duan et al., 2022), while studies in northern-Central Ecuador have settled on a broader time frame (e.g., Cochrane et al., 2014; Spikings et al., 2015), with migration thought to have occurred between the Jurassic and Early Cretaceous (see Section 4.2). These interpretations are based on the presence of Early Cretaceous magmatic units located west of older arc remnants. For example, the Peltetec Complex, which has traditionally be interpreted as Early Cretaceous (~134 Ma) based on $^{40}Ar/^{39}Ar$ dating on hornblende, muscovite, and biotite (Gabriele, 2002; Spikings et al., 2015), is emplaced to the west of Jurassic batholiths. However, Villares et al. (2020) proposed a Triassic age of 228.1 ± 1.7 Ma for the Complex using U—Pb dating and suggested that the $^{40}Ar/^{39}Ar$ ages reflect a Cretaceous thermal overprint associated with high-pressure metamorphism (~130 Ma; Gabriele, 2002; Riel et al., 2014), challenging the previously proposed Jurassic timing (~194 Ma) for arc migration.

Further south (8°–18.4°S), Martínez-Ardila et al. (2023) identified a progressive eastward migration of the Mesozoic arc through central and southern Peru (see Fig. 3C). The ages of Mesozoic rocks became increasingly younger toward the foreland between 200 and 66 Ma. This trend, in opposition to the westward migration observed in our study area, highlights the complex geodynamic evolution of the Andean arc as well as the regional variability in subduction processes during the Mesozoic.

5.4. Middle-late cretaceous evolution: The formation of a distinct arc

During the Albian (~100 Ma), active seafloor spreading in the South Atlantic Ocean and the westward drift of the South American Plate marked a shift from a predominantly extensional regime toward a compressional, Andean-type subduction system. This change in plate dynamics promoted the establishment of a new continental arc (Fig. 12E; Jaillard et al., 2000). This interpretation is supported by our U—Pb data (Fig. 3; Table 5), which records ages (100.8–87.8 Ma) that are consistent with those reported by Winter (2008) (U—Pb in zircon; 100.2 ± 0.5 to 78.6 ± 1.9 Ma).

Late Cretaceous magmatism produced rocks with a broad range of SiO_2 contents (Table S8), ranging from metaluminous to peraluminous rocks (Fig. 6D) from diorite to granite as well as minor occurrences of silica-undersaturated gabbros (Fig. 6A). Notably, the gabbro sample (IG22–18), one of the easternmost samples in the Late Cretaceous dataset, stands out due to its primitive character. Despite its juvenile isotopic signature (εHf > +10; Table S9), zircon analyses reveal very high U/Yb ratios (~5–7), typical of crustal assimilation and fluid-enriched mantle sources. These paradox results suggest that this gabbro is an enigmatic product of hydrous mantle melting in a continental arc setting, akin to tholeiitic gabbros in the Eastern Pontides Orogenic Belt (NE Turkey), where similar primitive but high-U/Yb magmas are attributed to bimodal arc magmatism (Temizel et al., 2022). Alternatively, the combination of high εHf and elevated U/Yb in this gabbro may reflect a juvenile parental magma generated under garnet- or amphibole-controlled melting conditions that suppressed Yb.

The whole-rock compositions of these samples are characteristic of calc-alkaline and calcic signatures (Fig. 6E), with magnesian affinities (Fig. 6F). This marks a change from the Early Cretaceous, when compositions ranged from magnesian to ferroan. These geochemical trends may reflect the influence of the newly established compressional setting, which likely contributed to increased crustal thickening and differentiation, thus favoring magnesian, calcic-alkalic compositions (e.g., Frost and Frost, 2008). However, Dy/Yb ratios in zircon remain consistently low, while LREE/HREE ratios remain highly variable, with samples exhibiting particularly high values, indicative of a magmatic source formed under conditions where garnet was absent (Fig. 10B). Nevertheless, the Dy/Yb ratios increase around 93 Ma, suggesting higher-pressure melting conditions consistent with the stabilization of garnet in the residue, and therefore with magma generation at greater crustal depths. This combination may reflect progressive crustal thickening and differentiation under a developing compressional regime. While these geochemical shifts are potential evidence of a tectonic transition, additional data are required to determine whether significant crustal thickening occurred during this period.

Zircon Th/U ratios (Fig. 9B) can be categorized into two distinct groups: (i) an intermediate group (Th/U ratios of 0.3–1) associated with felsic compositions, and (ii) a high-Th/U group (Th/U ratios >1.5), typically associated with more mafic magmatism. This distribution is consistent with the zircon Nb/Ta ratios (Fig. 10D), which possess values that are more characteristic of mafic sources, highlighting the significant influence of such components in the Late Cretaceous magmatic system. The broad distribution of U/Yb ratios (Fig. 10A) is indicative of contributions from both MORB sources and enriched mantle or crustal inputs. The coexistence of oceanic and continental zircon signatures (Fig. 9C and D), as well as I-type and hybrid S-type granitoid affinities, provides further support for a mixed-source model. This is also evidenced by zircon isotopic data: highly depleted $\varepsilon\mathrm{Hf}_{(t)}$ values, in some cases approaching the depleted mantle (DM) field (Fig. 8A), occur together with predominantly mantle-like $\delta^{18}O$ signatures, while a few low $\delta^{18}O$ values (<4.4 ‰) are present as outliers. These features are best explained by mantle input combined with limited assimilation or partial melting of gabbroic photoliths (Valley et al., 2005), mixing model, consistent with a mixing scenario.

Consequently, our data indicate that the Late Cretaceous arc was constructed on an oceanic basement. Potential origins for this basement include: (i) the underplated Early Cretaceous Raspas Ophiolitic Complex (Riel et al., 2014); (ii) inherited Paleozoic–Triassic oceanic crust, preserved as fragments of lithosphere generated during the Late Permian–Triassic breakup of Pangea, consistent with models proposed for the Western Peruvian Trough (ca. 9–12°S; Polliand et al., 2005); or (iii) new oceanic crust formed through mantle upwelling and melting during the opening of the Celica–Lancones Basin. The third scenario is considered less likely, as the Celica–Lancones arc occupies a forearc position where basaltic magmatism is typically linked to incipient subduction, an interpretation that conflicts with the evidence presented here for continuous subduction since the Triassic. Ultimately, the spatial distribution of our dataset remains insufficient to unambiguously resolve the precise origin of this oceanic basement.

Regardless of mechanism, the Celica–Lancones arc spans the Late Albian to Turonian (100–88 Ma) and could be considered to be the northern counterpart of the Aptian–Albian volcanic arc of Peru due to their coeval magmatism. However, these arcs differ in terms of their basement characteristics: the central–southern Peruvian arc was emplaced on continental crust (Martínez-Ardila et al., 2023; Soler, 1991), while it is clear that the Celica–Lancones Arc is emplaced on oceanic crust. Despite their similar timing, these differences suggest that the two arcs evolved under distinct tectonic conditions, highlighting the complexity of magmatic arcs along the same subduction margin.

This work shows that the integration of U—Pb geochronology, whole-rock geochemistry, and zircon εHf and $\delta^{18}O$ isotopic data is a powerful tool for reconstructing the spatial and temporal evolution of magmatic arcs. The analyses presented here demonstrate that this approach is particularly effective in highly dynamic subduction systems, where the formation of distinct crustal domains can strongly influence arc geochemistry.

6. Conclusions

The U—Pb zircon data presented in this study refine the existing geochronological framework of Mesozoic magmatism in southern Ecuador and northern Peru, providing new insights into the spatiotemporal evolution of the arc. Triassic magmatism occurred in an active subduction setting. Between 240 and 220 Ma, magmatism was characterized by significant crustal recycling and the formation of S-type granitoids as indicated by zircon Hf—O isotopic data that indicate sustained crustal assimilation until at least 220 Ma. Post-Triassic magmatism marked a transition to voluminous I-type granitoids emplacement, while Jurassic magmatism (201–157 Ma) occurred under an extensional arc system, characterized by a shift toward less radiogenic isotopic compositions, reflecting an increasing contribution from juvenile mantle sources. In addition, the new Jurassic ages obtained in this study challenge the interpretation of a missing Jurassic arc in northern Peru, suggesting that magmatic activity may have been more widespread than previously thought. Furthermore, the synchronous nature of the Jurassic magmatism in southern Ecuador, northern Peru, and Colombia challenges the previously proposed southward-younging trend for the region.

Changes in subduction geometry in the Early Cretaceous had an influence on magmatic activity during this period, favoring the melting of primarily mantle sources. The magmatic arc remained stationary and active between ~190 and ~ 126 Ma, but by the Middle Cretaceous, the arc had migrated westward, likely due to slab rollback. This coincided with the formation of the Celica–Lancones Basin, contradicting previous interpretations of Jurassic–Early Cretaceous arc migration.

During the Late Cretaceous (~100 to ~88 Ma), magmatism evolved within a compressional regime and involved contributions from oceanic-like components. This oceanic signature may have been derived from (i) the melting of a lower crustal material, possibly linked to the underplated Early Cretaceous Raspas Ophiolitic Complex; (ii) direct input from an upwelling depleted mantle, forming an oceanic-like basement during the opening of the Celica–Lancones Basin; or (iii) melting of preserved fragments of lithosphere generated during the Late Permian–Triassic breakup of Pangea.

Supplementary data to this article can be found online at https://doi.org/10.1016/j.lithos.2025.108389.

Funding sources

This work was supported by the PhD scholarship awarded to Leidy Carolina Sandoval Espinel by the University of Padova (Grand: 2077712).

CRediT authorship contribution statement

Leidy Carolina Sandoval Espinel: Writing – original draft, Visualization, Methodology, Formal analysis, Conceptualization. **Cesar Witt:** Writing – review & editing, Supervision, Formal analysis, Conceptualization. **Jorge Iglesias:** Writing – review & editing, Methodology. **Massimiliano Zattin:** Writing – review & editing, Supervision, Formal analysis. **Olivier Bruguier:** Writing – review & editing, Data curation. **Marc Poujol:** Writing – review & editing, Data curation. **Pablo Samaniego:** Writing – review & editing. **Mauricio Bermudez:** Writing – review & editing, Supervision, Formal analysis. **John Jairo Sandoval Espinel:** Writing – review & editing, Visualization, Methodology.

Declaration of competing interest

The authors declare that they have no known competing financial interests or personal relationships that could have appeared to influence the work reported in this paper.

Acknowledgments

We thank Leonardo Tauro for his assistance with the preparation of thin sections at the University of Padova. We are also grateful to Editor-in-Chief Greg Shellnutt, reviewer Alina Tibaldi, and an anonymous reviewer for their thoughtful and constructive comments, which greatly improved the quality and clarity of this manuscript.

References

Aspen, J.A., Fornari, M., Litherland, M., Viteri, E., Harrison, S.M., 1992. Regional S-type granites in the Ecuadorian Andes: possible remnants of the breakup of western Gondwana. South Am. Earth Sci. 6, 123–132.

Attia, S., Cottle, J.M., Paterson, S.R., 2020. Erupted zircon record of continental crust formation during mantle driven arc flare-ups. Geology 48 (5), 446–451. https://doi.org/10.1130/G46991.1 %J Geology.

Baldock, J.W., 1977. Low-Density Geochemical Reconnaissance in Peru to Delineate Individual Mineral Deposits. Institution of Mining and Metallurgy. Transactions. Section B, Applied Earth Sciences, pp. 63–72.

Barragán, R., Baby, P., Duncan, R., 2005. Cretaceous alkaline intra-plate magmatism in the Ecuadorian Oriente Basin: Geochemical, geochronological and tectonic evidence. Earth Planet. Sci. Lett. 236 (3), 670–690. https://doi.org/10.1016/j.epsl.2005.03.016.

Bayona, G., Bustamante, C., Nova, G., Salazar-Franco, A.M., 2020. Jurassic evolution of the northwestern corner of Gondwana: Present knowledge and future challenges in studying Colombian Jurassic rocks. In: Gómez, J.P.P. (Ed.), The geology of Colombia, Servicio Geológico Colombiano, Publicaciones Geológicas Especiales, 2, pp. 171–207. https://doi.org/10.32685/pub.esp.36.2019.05, 36.

Belousova, E., Griffin, W., O'Reilly, S.Y., Fisher, N., 2002. Igneous zircon: trace element composition as an indicator of source rock type. Contrib. Mineral. Petrol. 143 (5), 602–622. https://doi.org/10.1007/s00410-002-0364-7.

Blichert-Toft, J., 2008. The Hf isotopic composition of zircon reference material 91500. Chem. Geol. 253 (3–4), 252–257. https://doi.org/10.1016/j.chemgeo.2008.05.014.

Boekhout, F., Spikings, R., Sempere, T., Chiaradia, M., Ulianov, A., Schaltegger, U., 2012. Mesozoic arc magmatism along the southern Peruvian margin during Gondwana breakup and dispersal. Lithos 146-147, 48–64. https://doi.org/10.1016/j.lithos.2012.04.015.

Bustamante, C., Archanjo, C.J., Cardona, A., Vervoort, J.D., 2016. Late Jurassic to early cretaceous plutonism in the Colombian Andes: a record of long-term arc maturity. GSA Bull. 128 (11–12), 1762–1779. https://doi.org/10.1130/B31307.1.

Carrasco, H., Spikings, R., Chiaradia, M., Ulianov, A., Buenaño, P., Zambrano, A., Beate, B., 2023. Geochronological, geochemical and isotopic characterisation of the early cretaceous Andean margin within Ecuador: the Alao Arc. Lithos 462-463, 107400. https://doi.org/10.1016/j.lithos.2023.107400.

Carrillo, E., Barragán, R., Hurtado, C., Calderón, Y., Martín, G., Vázquez-Taset, Y., Sarmiento, L., 2021. Depositional sequences in northern Peru: new insights on the palaeogeographic and palaeotectonic reconstruction of western Gondwana during late Permian and Triassic. J. Geol. Soc. *178* (6). https://doi.org/10.1144/jgs2020-186.

CGS_INGEMMET, 2017. Convenio de Cooperación entre el Servicio Geologico de China e INGEMMET.

Chapman, J.B., Ducea, M.N., DeCelles, P.G., Profeta, L., 2015. Tracking changes in crustal thickness during orogenic evolution with Sr/Y: an example from the north American Cordillera. Geology 43 (10), 919–922. https://doi.org/10.1130/G36996.1.

Chavarría, L., Bustamante, C., Cardona, A., Bayona, G., 2022. Quantifying crustal thickness and magmatic temperatures of the Jurassic to early cretaceous North-Andean arc. Int. Geol. Rev. 64 (18), 2544–2564. https://doi.org/10.1080/00206814.2021.1992301.

Chiaradia, M., 2009. Adakite-like magmas from fractional crystallization and melting-assimilation of mafic lower crust (Eocene Macuchi arc, Western Cordillera, Ecuador). Chem. Geol. 265 (3–4), 468–487. https://doi.org/10.1016/j.chemgeo.2009.05.014.

Chiaradia, M., Vallance, J., Fontboté, L., Stein, H., Schaltegger, U., Coder, J., Gendall, I., 2009. U–Pb, Re–Os, and 40Ar/39Ar geochronology of the Nambija Au-skarn and Pangui porphyry Cu deposits, Ecuador: implications for the Jurassic metallogenic belt of the Northern Andes. Mineral. Deposita 44 (4), 371–387. https://doi.org/10.1007/s00126-008-0210-6.

Cochrane, R.S.J., 2013. U-Pb thermochronology, geochronology and geochemistry of NW South America: rift to drift transition, active margin dynamics and implications for the volume balance of continents. Université de Genève.

Cochrane, R., Spikings, R., Gerdes, A., Ulianov, A., Mora, A., Villagómez, D., Chiaradia, M., 2014. Permo-Triassic anatexis, continental rifting and the disassembly of western Pangaea. Lithos 190-191, 383–402. https://doi.org/10.1016/j.lithos.2013.12.020.

Coder, J., 2003. Geologic Setting, Geochronologic Relationships, And Lithogeochemistry Of The Pangui Porphyry Copper District, Southeast Ecuador.

Cotten, J., Le Dez, A., Bau, M., Caroff, M., Maury, R.C., Dulski, P., Brousse, R., 1995. Origin of anomalous rare-earth element and yttrium enrichments in subaerially exposed basalts: evidence from French Polynesia. Chem. Geol. 119 (1), 115–138. https://doi.org/10.1016/0009-2541(94)00102-E.

DeCelles, P.G., Ducea, M.N., Kapp, P., Zandt, G., 2009. Cyclicity in Cordilleran orogenic systems. Nat. Geosci. 2 (4), 251–257. https://doi.org/10.1038/ngeo469.

Drabon, N., Kirkpatrick, H.M., Byerly, G.R., Wooden, J.L., 2024. Trace elements in zircon record changing magmatic processes and the multi-stage build-up of Archean proto-continental crust. Geochim. Cosmochim. Acta 373, 136–150. https://doi.org/10.1016/j.gca.2024.03.014.

Drobe, J., Lindsay, D., Stein, H., Gabites, J., 2013. Geology, mineralization, and geochronological constraints of the mirador Cu-Au Porphyry District Southeast Ecuador. Soc. Econ. Geolog. 106, 11–35.

Duan, Z., Guo, W.-M., Xiang, H.-L., Liu, J.-A., Jaimes, F., Astete, I., 2022. Geochronology and geochemistry of Early Cretaceous volcanic sequences in Northwestern Peru: implications for Farallon Plate subduction. Int. Geol. Rev. 64 (22), 3171–3194. https://doi.org/10.1080/00206814.2021.2024769.

Ducea, M.N., Saleeby, J.B., Bergantz, G., 2015. The Architecture, Chemistry, and Evolution of Continental Magmatic Arcs. Annu. Rev. Earth Planet. Sci. 43 (1), 299–331. https://doi.org/10.1146/annurev-earth-060614-105049.

Feininger, T., Silberman, M.L., 1982. *K-Ar geochronology of basement rocks on the northern flank of the Huancabama deflection, Ecuador* [Report](82-206). Open-File Report, Issue. U. S. G. Survey. https://pubs.usgs.gov/publication/ofr82206.

Frost, B.R., Frost, C.D., 2008. A Geochemical Classification for Feldspathic Igneous Rocks. J. Petrol. 49 (11), 1955–1969. https://doi.org/10.1093/petrology/egn054.

Frost, C.D., Frost, B.R., 2023. Petrologic constraints on the origin of Proterozoic ferroan granites of the Laurentian margin. In: Laurentia: Turning Points in the Evolution of a Continent, vol. 220. Geological Society of America, p. 0. https://doi.org/10.1130/2022.1220(10).

Gabriele, P., 2002. HP Terranes Exhumation in an Active Margin Setting: Geology, Petrology and Geochemistry of the Raspas Complex in SW Ecuador. Univ of Lausanne.

Gendall, I.R., Quevedo, L.A., Sillitoe, R.H., Spencer, R.M., Puente, C.O., LeÓN, J.P., Pvedo, R.R., 2000. Discovery of a Jurassic Porphyry Copper Belt, Pangui Area, Southern Ecuador. SEG Discovery 43, 1–15. https://doi.org/10.5382/SEGnews.2000-43.fea.

Gonfiantini, R., Stichler, W., Rozanski, K., 1995. *Standards and Intercomparison Materials Distributed by the International Atomic Energy Agency for Stable Isotope Measurements* (IAEA).

Grimes, C.B., John, B.E., Kelemen, P.B., Mazdab, F.K., Wooden, J.L., Cheadle, M.J., Schwartz, J.J., 2007. Trace element chemistry of zircons from oceanic crust: a method for distinguishing detrital zircon provenance. Geology 35 (7). https://doi.org/10.1130/g23603a.1.

Grimes, C.B., Wooden, J.L., Cheadle, M.J., John, B.E., 2015. Fingerprinting tectono-magmatic provenance using trace elements in igneous zircon. Contrib. Mineral. Petrol. 170 (5–6). https://doi.org/10.1007/s00410-015-1199-3.

Guo, P., Yang, T., 2023. Quantifying continental crust thickness using the machine learning method. J. Geophys. Res. Solid Earth 128 (3). https://doi.org/10.1029/2022JB025970 e2022JB025970.

Hama, H., 1990. *Report on the Mineral Exploration in the Pachapiriana Area Republic of Peru - Phase II* Codigo A3343 (Issue).

Horton, B.K., 2018. Sedimentary record of Andean mountain building. Earth Sci. Rev. 178, 279–309. https://doi.org/10.1016/j.earscirev.2017.11.025.

Hoskin, P.W.O., Schaltegger, U., 2003. The composition of zircon and igneous and metamorphic petrogenesis. Rev. Mineral. Geochem. 53, 25–104.

Iglesias, J., Witt, C., Poma, O., Bruguier, O., Bosch, D., Bosse, V., Averbuch, O., 2025. Geochronology and geochemistry of Cenozoic magmatism in the north-western Ecuadorian Andes: the role of crustal thickness. Lithos 514-515, 108159. https://doi.org/10.1016/j.lithos.2025.108159.

Jaillard, E., 2022. Late cretaceous-paleogene orogenic build-up of the Ecuadorian Andes: Review and discussion. Earth Sci. Rev. 230. https://doi.org/10.1016/j.earscirev.2022.104033.

Jaillard, E., 2025. Did the evolution from oblique to normal convergence contribute to the Andean building? J. S. Am. Earth Sci. 152, 105312. https://doi.org/10.1016/j.jsames.2024.105312.

Jaillard, E., Soler, P., 1996. Cretaceous to early Paleogene tectonic evolution of the northern Central Andes (0–18°S) and its relations to geodynamics. Tectonophysics 259 (1), 41–53. https://doi.org/10.1016/0040-1951(95)00107-7.

Jaillard, E., Soler, P., Carlier, G., Mourier, T., 1990. Geodynamic evolution of the northern and Central Andes during early to middle Mesozoic times: a Tethyan model. J. Geol. Soc. Lond. 147 (6), 1009–1022. https://doi.org/10.1144/gsjgs.147.6.1009.

Jaillard, E., Laubacher, G., Bengtson, P., Dhondt, A.V., Bulot, L., 1999. Stratigraphy and evolution of the cretaceous forearc Celica-Lancones basin of southwestern Ecuador. J. S. Am. Earth Sci. 12, 51–68.

Jaillard, E., Herail, G., Monfret, T., Diaz-Martinez, E., Baby, P., Lavenu, A., Dumont, J., 2000. Tectonic evolution of the Andes of Ecuador, Peru, Bolivia and northernmost Chile. Tectonic Evolut. South America 481–559.

Leal-Mejía, H., Shaw, R.P., Melgarejo Draper, J.C., 2019. Spatial-Temporal migration of granitoid magmatism and the Phanerozoic tectono-magmatic evolution of the Colombian Andes. In: Cediel, F., Shaw, R.P. (Eds.), Geology and Tectonics of Northwestern South America: The Pacific-Caribbean-Andean Junction. Springer International Publishing, pp. 253–410. https://doi.org/10.1007/978-3-319-76132-9_5.

Litherland, M., 1994. The metamorphic belts of Ecuador. Overseas Memoir 11, 1–147.

Maloney, K.T., Clarke, G.L., Klepeis, K.A., Quevedo, L., 2013. The late Jurassic to present evolution of the Andean margin: drivers and the geological record. Tectonics 32 (5), 1049–1065. https://doi.org/10.1002/tect.20067.

Martínez-Ardila, A.M., Pompe, L., Clausen, B.L., Paterson, S.R., Holk, G.J., Luffi, P., 2023. A synthesis of the Peruvian Coastal Batholith: an exploration of temporal histories, causes of compositional diversity, and tectonomagmatic links in arcs. Lithos 456-457, 107298. https://doi.org/10.1016/j.lithos.2023.107298.

Mišković, A., Spikings, R.A., Chew, D.M., Košler, J., Ulianov, A., Schaltegger, U., 2009. Tectonomagmatic evolution of Western Amazonia: Geochemical characterization and zircon U-Pb geochronologic constraints from the Peruvian Eastern Cordilleran granitoids. Geol. Soc. Am. Bull. 121 (9–10), 1298–1324. https://doi.org/10.1130/b26488.1.

Morel, M.L.A., Nebel, O., Nebel-Jacobsen, Y.J., Miller, J.S., Vroon, P.Z., 2008. Hafnium isotope characterization of the GJ-1 zircon reference material by solution and laser-ablation MC-ICPMS. Chem. Geol. 255 (1–2), 231–235. https://doi.org/10.1016/j.chemgeo.2008.06.040.

Mourier, T., 1988. Transición entre Andes marginales y Andes cordilleranos: evolución sedimentaria, magmática y estructural deflexión de Huancabamba: 3° a 8° Lat. S; Norte del Perú y Sur de Ecuador. Universidad de Paris Sur.

Pearce, N.J.G., Perkins, W.T., Westgate, J.A., Gorton, M.P., Jackson, S.E., Neal, C.R., Chenery, S.P., 2007. A Compilation of New and published Major and Trace Element Data for NIST SRM 610 and NIST SRM 612 Glass Reference Materials. Geostand. Newslett. 21 (1), 115–144. https://doi.org/10.1111/j.1751-908X.1997.tb00538.x.

Polliand, M., Schaltegger, U., Frank, M., Fontbot, L., 2005. Formation of intra-arc volcanosedimentary basins in the western flank of the central Peruvian Andes during late cretaceous oblique subduction: field evidence and constraints from U-Pb ages and Hf isotopes. Int. J. Earth Sci. 94 (2), 231–242. https://doi.org/10.1007/s00531-005-0464-5.

Pratt, W.T., Duque, P., Ponce, M., 2005. An autochthonous geological model for the eastern Andes of Ecuador. Tectonophysics 399 (1), 251–278. https://doi.org/10.1016/j.tecto.2004.12.025.

Profeta, L., Ducea, M.N., Chapman, J.B., Paterson, S.R., Gonzales, S.M., Kirsch, M., DeCelles, P.G., 2015. Quantifying crustal thickness over time in magmatic arcs. Sci. Rep. 5, 17786. https://doi.org/10.1038/srep17786.

Ramos, V.A., 2009. Anatomy and global context of the Andes: Main geologic features and the Andean orogenic cycle. In: *Backbone of the Americas:* Shallow Subduction, Plateau Uplift, and Ridge and Terrane Collision. https://doi.org/10.1130/2009.1204(02).

Riel, N., Martelat, J.-E., Guillot, S., Jaillard, E., Monié, P., Yuquilema, J., Mercier, J., 2014. Fore arc tectonothermal evolution of the El Oro metamorphic province (Ecuador) during the Mesozoic. Tectonics 33 (10), 1989–2012. https://doi.org/10.1002/2014TC003618.

Riel, N., Jaillard, E., Martelat, J.-E., Guillot, S., Braun, J., 2018. Permian-Triassic Tethyan realm reorganization: Implications for the outward Pangea margin. J. S. Am. Earth Sci. 81, 78–86. https://doi.org/10.1016/j.jsames.2017.11.007.

Roberts, N.M.W., Yakymchuk, C., Spencer, C.J., Keller, C.B., Tapster, S.R., 2024. Revisiting the discrimination and distribution of S-type granites from zircon trace element composition. Earth Planet. Sci. Lett. 633, 118638. https://doi.org/10.1016/j.epsl.2024.118638.

Sandoval-Espinel, L.C., Witt, C., Zattin, M., Poujol, M., Bruguier, O., Chiaradia, M., Bermudez, M., 2025. Pervasive crustal reworking along the proto-Andean margin of northern Peru and southern Ecuador: Insights from U-Pb, geochemical, and isotopic analyses of zircon. J. S. Am. Earth Sci. 158, 105502. https://doi.org/10.1016/j.jsames.2025.105502.

Schütte, P., Chiaradia, M., Beate, B., 2010. Geodynamic controls on Tertiary arc magmatism in Ecuador: Constraints from U–Pb zircon geochronology of Oligocene–Miocene intrusions and regional age distribution trends. Tectonophysics 489 (1–4), 159–176. https://doi.org/10.1016/j.tecto.2010.04.015.

Sláma, J., Košler, J., Condon, D.J., Crowley, J.L., Gerdes, A., Hanchar, J.M., Whitehouse, M.J., 2008. Plešovice zircon — A new natural reference material for U–Pb and Hf isotopic microanalysis. Chem. Geol. 249 (1–2), 1–35. https://doi.org/10.1016/j.chemgeo.2007.11.005.

Soler, P., 1991. Contibution à l'etude du magmatisme associé aux zones de subduction. Pétrographie, géochimie et géchimie isotopique des roches intrusives sur un transect des Andes du Pérou Central. Implucations géeodynamiques et métallogéeniques. Univ. Paris.

Spikings, R.A., Crowhurst, P.V., Winkler, W., Villagomez, D., 2010. Syn- and post-accretionary cooling history of the Ecuadorian Andes constrained by their in-situ and detrital thermochronometric record. J. S. Am. Earth Sci. 30 (3), 121–133. https://doi.org/10.1016/j.jsames.2010.04.002.

Spikings, R., Cochrane, R., Villagomez, D., Van der Lelij, R., Vallejo, C., Winkler, W., Beate, B., 2015. The geological history of northwestern South America: from Pangaea to the early collision of the Caribbean large Igneous Province (290–75 Ma). Gondwana Res. 27, 95–139. https://doi.org/10.1016/j.gr.2014.06.004.

Teipel, U., Eichhorn, R., Loth, G., Rohrmüller, J., Höll, R., Kennedy, A., 2004. U-Pb SHRIMP and Nd isotopic data from the western Bohemian Massif (Bayerischer Wald, Germany): implications for Upper Vendian and lower Ordovician magmatism. Int. J. Earth Sci. 93 (5), 782–801. https://doi.org/10.1007/s00531-004-0419-2.

Temizel, İ., Arslan, M., Abdioğlu Yazar, E., Aslan, Z., Kaygusuz, A., Baki Eraydın, T., 2022. Zircon UPb geochronology and petrology of the tholeiitic gabbro from the Kovanlık (Giresun) area: Constraints for the late cretaceous bimodal arc magmatism in the Eastern Pontides Orogenic Belt NE Turkey. Lithos 428-429, 106840. https://doi.org/10.1016/j.lithos.2022.106840.

Urlich, T., 2005. Summary Report on Ar/Ar Dating for MAP: GAC. *Activity PE–05 Peru.* Laboratory Pacific Centre for Isotopic Geochemical Research Earth Ocean Sciences. University of British Columbia, Vancouver.

Vallejo, C., Winkler, W., Spikings, R.A., Luzieux, L., Heller, F., Bussy, F., 2009. Mode and timing of terrane accretion in the forearc of the Andes in Ecuador. In: *Backbone of the Americas:* Shallow Subduction, Plateau Uplift, and Ridge and Terrane Collision. https://doi.org/10.1130/2009.1204(09).

Valley, J.W., Lackey, J.S., Cavosie, A.J., Clechenko, C.C., Spicuzza, M.J., Basei, M.A.S., Wei, C.S., 2005. 4.4 billion years of crustal maturation: oxygen isotope ratios of magmatic zircon. Contrib. Mineral. Petrol. 150 (6), 561–580. https://doi.org/10.1007/s00410-005-0025-8.

van Achterberg, E., Ryan, C.G., Jackson, S.E., Griffin, W.L., 2001. Data reduction software for LA-ICP-MS : Appendix. In: Sylvester, P.J. (Ed.), Laser Ablation-ICP- Mass Spectrometry in the Earth Sciences: Principles and Applications. Mineralogical Association of Canada, Short Course Series, Ottawa, Ontario, Canada, pp. 239–243.

Van der Lelij, R., 2013. Reconstructing North-Western Gondwana with Implications for the Evolution of the Iapetus and Rheic Oceans: A Geochronological, Thermochronological and Geochemical Study (Publication Number 4581). University Genève.

Verma, S.P., Rivera-Gómez, M.A., 2013. Computer programs for the classification and nomenclature of igneous rocks. Int. Union Geolog. Sci. 36 (2), 115–124. https://doi.org/10.18814/epiiugs/2013/v36i2/005.

Vervoort, J.D., Blichert-Toft, J., 1999. Evolution of the depleted mantle: Hf isotope evidence from juvenile rocks through time. Geochim. Cosmochim. Acta 63 (3), 533–556. https://doi.org/10.1016/S0016-7037(98)00274-9.

Villagómez, D., Spikings, R., Magna, T., Kammer, A., Winkler, W., Beltrán, A., 2011. Geochronology, geochemistry and tectonic evolution of the Western and Central cordilleras of Colombia. Lithos 125 (3), 875–896. https://doi.org/10.1016/j.lithos.2011.05.003.

Villares, F., Garcia-Casco, A., Blanco-Quintero, I.F., Montes, C., Reyes, P.S., Cardona, A., 2020. The Peltetec ophiolitic belt (Ecuador): a window to the tectonic evolution of the Triassic margin of western Gondwana. Int. Geol. Rev. 63 (18), 2232–2256. https://doi.org/10.1080/00206814.2020.1830313.

Winter, L., 2008. The Genesis of Giant Copper-Zing-Gold-Silver Volcanogenic Massive Sulphide Deposits at Tambogrande, Peru: Age, Tectonic Setting, Paleomorphology, Lithogeochemistry and Radiogenic Isotopes. University of British Columbia.

Winter, L.S., Tosdal, R.M., Mortensen, J.K., Franklin, J.M., 2010. Volcanic stratigraphy and geochronology of the Cretaceous Lancones Basin, Northwestern Peru: Position and timing of Giant VMS Deposits. Econ. Geol. 105 (4), 713–742. https://doi.org/10.2113/gsecongeo.105.4.713 %J Economic Geology.

Witt, C., Rivadeneira, M., Poujol, M., Barba, D., Beida, D., Beseme, G., Montenegro, G., 2017. Tracking ancient magmatism and Cenozoic topographic growth within the Northern Andes forearc: Constraints from detrital U-Pb zircon ages. Geol. Soc. Am. Bull. 129 (3–4), 415–428. https://doi.org/10.1130/b31530.1.

Witt, C., Poujol, M., Chiaradia, M., Villagomez, D., Seyler, M., Averbuch, O., Bouden, N., 2023. Geodynamic controls in the southernmost Northern Andes magmatic arc: Trace elements and Hf-O isotopic systematics in forearc detrital zircon. GSA Bull. https://doi.org/10.1130/b36510.1.